INCREASING THE ACCURACY OF BRAIN FUNCTIONAL MAPS THROUGH LARGE DEFORMATION DIFFEOMORPHIC METRIC MAPPING

by

Behrang Nosrat Makouei

B.A.Sc., Sharif University of Technology, 2004

A THESIS SUBMITTED IN PARTIAL FULFILLMENT
OF THE REQUIREMENTS FOR THE DEGREE OF
MASTER OF APPLIED SCIENCE
in the School
of
Engineering Science

SIMON FRASER UNIVERSITY
Spring 2008

APPROVAL

Name: Behrang Nosrat Makouei

Degree: Master of Applied Science

Title of thesis : Increasing The Accuracy Of Brain Functional Maps Through Large Deformation Diffeomorphic Metric Mapping

Examining Committee:

Dr. Rodney G. Vaughan
Professor, School of Engineering Science
Chair

Dr. Mirza Faisal Beg, Senior Supervisor
Assistant Professor, School of Engineering Science

Dr. Lei Wang, Supervisor
Research Assistant Professor, Psychiatry
Washington University School of Medicine, St. Louis

Dr. Anthony Herdman, Supervisor
Assistant Professor, Department of Psychology

Dr. Yue Wang, Internal Examiner
Assistant Professor, Department of Linguistics

Date Approved: March 25, 2008

Abstract

The accuracy of the brain normalization method directly impacts the preciseness of statistical analysis of functional magnetic resonance imaging (fMRI) data. Furthermore, the study of the medial temporal lobe and cortical layer structures requires an accurate co-registration method due to large inter-subject variability. In this thesis, we first introduce a fully automated fMRI post-processing pipeline aimed to reduce the registration error during group studies and we will demonstrate its superiority over two widely used registration methods by conducting a comprehensive bleeding study using a synthesized fMRI data-set as well as surface-to-surface distance quantifications over both cortical and sub-cortical regions. Finally, we apply our processing pipeline to a functional MRI data-set of a schizophrenia study and show how accurate registration of hippocampus and inferior frontal gyrus structures can increase the accuracy of functional maps over these regions when performing group analysis.

Keywords: functional MRI; spatial normalization; BOLD fMRI; brain normalization; computational anatomy; schizophrenia

To my family, friends and teachers

"Man is descended from a hairy, tailed quadruped, probably arboreal in its habits."

CHARLES DARWIN

Contents

List of Tables

List of Figures

Chapter 1

Introduction

During late 1980*s* only a handful of research groups were performing human brain activation studies using ionizing radiation or electroencephalography (EEG). When functional magnetic resonance imaging (fMRI) came into common use in early 1990s and its superior flexibility and degrees of freedom over the common brain mapping techniques were realized by the researchers, a breakthrough was happening in brain mapping experiments. After mid 1990*s* when the first fMRI papers were published, researchers could perform brain mapping studies relatively easily: have the subject in the scanner, ask the subject to perform a task and then look for activation maps of the brain. Although extremely powerful, the newly available technology lead to a severe problem in the brain mapping community:

- A sudden rush to pick the scientific "low hanging fruit" lead to many poorly planned, executed and analyzed experiments and the associated published articles.

Although through major fMRI courses offered four to six times a year at Massachusetts General Hospital, twice a year at Medical College of Wisconsin and periodically elsewhere through the past decade have likely helped the increase in correctness of the fMRI experiments around the brain mapping community, there still exist major questions about the validity of the obtained results. Considering the vast number of fMRI experiments being undertaken and the related scientific articles being published (Fig. 1.1 shows the results of science citation index reference search on fMRI related articles published since 1992 till 2008), the goal of this thesis is to address one of the largely overlooked problems in fMRI group studies: *how brain normalization affects the statistical analysis results and how we can quantify the accuracy of the underlying normalization method.*

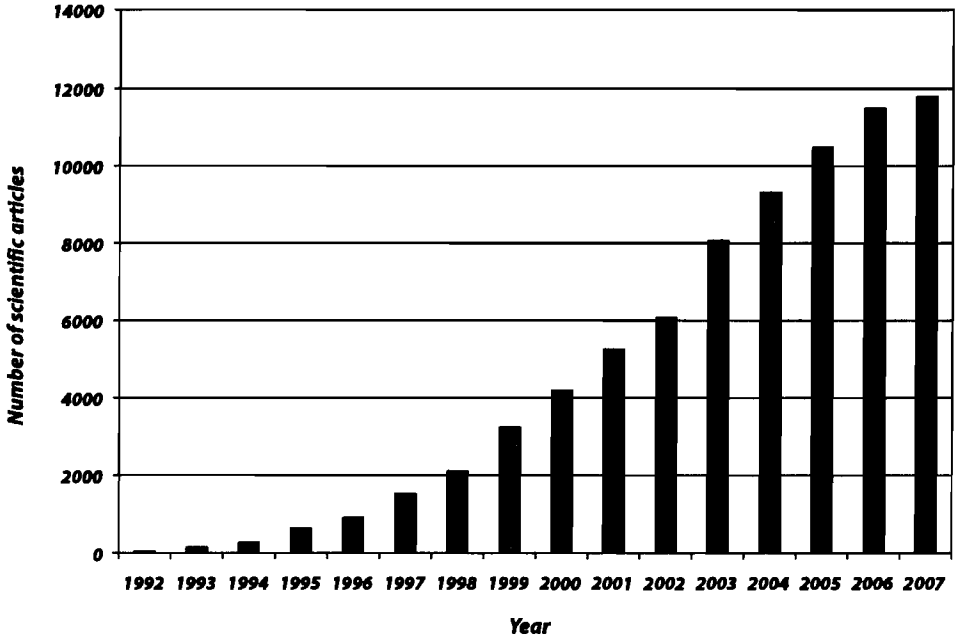

Figure 1.1: Number of fMRI related scientific articles published from 1992 till 2008 as searched for using Google Scholar and the search terms "fMRI" or "functional MRI".

This chapter starts with an introduction to magnetic resonance imaging in Section 1.1 followed by a short review of functional magnetic resonance imaging and the related topics in Section 1.2 and finally in Section 1.3 we will discuss the contributions of this thesis to the functional brain mapping community. In Chapter 2 we will describe our functional MRI processing pipeline together with the two other methods selected for comparison purposes. Later on Chapter 3 we will apply our method to a real functional data-set and compare the resulting statistical maps with the selected two other methods and finally Chapter 4 contains the conclusions of this thesis.

1.1 Magnetic Resonance Imaging

Magnetic resonance imaging (MRI) uses the signal from the nuclei of hydrogen atoms to generate images. The proton of the nuclei possessing spin has two properties:

- *angular momentum* striving to retain the spatial orientation of its rotation axis

- *magnetic moment* (B) behaving as a small magnet and identifying orientation of nuclies' rotation axis

Therefore, hydrogen nuclei are affected by external magnetic fields as well as electromagnetic waves and can induce a voltage in a receiver coil.

1.1.1 Larmor Frequency and Excitation

When the hydrogen nuclei is exposed to an external magnetic field, B_0, its magnetic moment aligns with the direction of the field. The alignment process is carried out in an oscillating fashion which determines the associated *Larmor or precession frequency.* Larmor frequency is proportional to the strength of the applied magnetic field and is given by

$$\omega_0 = \gamma_0 B_0$$

where γ_0 is the gyromagnetic ratio, a constant specific to a particular nucleus. Protons have a gyromagnetic ratio of $\gamma = 42.58$ MHz/T, resulting in a Larmor frequency of 63.9 MHz at 1.5T.

Spins tend to align parallel and anti-parallel to the external magnetic field with parallel alignment being slightly preferred as it results in spins residing in a more stable energy state. Hence, under steady state conditions, majority of the magnetic fields of the aligned nuclei cancel each other and small fraction being parallel to the external magnetic field, generate the net magnetization, M, which depends on the strength of B_0.

Using an *antenna coil*, if an electromagnetic wave of the same frequency as the Larmor frequency radiates to such an stable spin system (*resonance condition*), energy will be induced to the system. In this way, assuming B_0 and thus M are in the z direction, M will move from the longitudinal direction (z) towards the transverse (xy-) plane. The transverse magnetization (M_{xy}) rotates about the z-axis and can induce an alternating voltage of the same frequency as the Larmor frequency in a *receiver coil*; This induced signal is called the magnetic resonance (MR) signal.

After excitation by the RF pulse, the nuclei spins move towards their previous stable alignment with B_0 and thus the transverse magnetization (and the associated MR signal) rapidly fades. Returning of the nuclei spin is the result of two independent processes: spin-lattice interaction and spin-spin interactions. These two processes cause $T1$ and $T2$ *relaxations*, respectively.

1.1.2 T1 Relaxation

The excess energy injected by the RF pulse into the nuclei slowly fades as the nuclei return to the steady state by dissipating their excess energy to their surrounding *lattice* (which is why this kind of relaxation is also called spin-lattice relaxation). Through this process, the transverse component of M slowly vanishes as the longitudinal component of M returns to its original magnitude aligned with B_0. This process is known as *longitudinal relaxation* or $T1$ recovery. The time constant for this recovery, called $T1$, depends on the strength of the external magnetic field, B_0, and the internal Brownian motion of the molecules. Biological tissues have T1 values of half a second to several seconds at 1.5T.

1.1.3 T2 and T2* Relaxations

Right after excitation, the individual transverse components of the magnetization are rotating around the longitudinal component in an in-phase fashion. Energy transfer between spins will affect the coherence phase of M_{xy} components and spins will start to cancel out each other. Time constant associated with this process is called T2 and can be considered independent of the strength of B_0. Time-independent inhomogeneities of B_0 also contribute to the dephasing process with a shorter time constant called $T2^*$. While the effect of $T2^*$ can be reduced by the design of the imaging process, $T2$ is a characteristic of the tissue being imaged. $T1$ and $T2$ are completely independent but they occur more and less simultaneously. The effect of $T2$ relaxation can be observed within the first $100 \sim 300$msec while it takes $0.5 \sim 5$sec for the longitudinal component of M to recover due to the $T1$ relaxation.

1.1.4 Image Contrast and Spatial Resolution

Three intrinsic features of a biological tissue contribute to its signal intensity on an MR image:

- The $T1$ time of a tissue is the time it takes for the spins to recover from the excitation and be available for the next excitation. $T1$ affects the image density indirectly and images with contrasts that are mainly determined by $T1$ are called *T1-weighted images.* The contribution of $T1$ to image density can be controlled by the *repetition time (TR)* [1].

- The $T2$ time determines how fast the MR signal fades after excitation and can be controlled using the *echo time (TE)* [1]. Images with contrasts mainly determined by $T2$ are called *T2-weighted images.* It should be noted that, when magnetic imperfection effects are also parameterized in the image acquisition process, the resulting images are called $T2^*$ images.

- The proton density (the excitable spins per unit volume) can be emphasized in an MR image by minimizing the other two parameters, $T1$ and $T2$, and the acquired images are called *proton density images.*

The spatial coordinate of the acquired signal is controlled by the magnetic field gradients and the details are available from [1] and references within. Furthermore, without discussing the related details, it can be said that signal-to-noise ratio (SNR) of a MR image is mainly dependant on the following parameters:

- slice thickness and the receiver bandwidth
- field of view
- resolution of the image
- number of acquisitions
- scan parameters (TR, TE, flip angle)
- magnetic field strength
- RF coils

Although the resolution of the MR image and the SNR of the resulting image have, in some extent, an inverse relation, high SNR and high image resolution can be achieved by increasing the number of acquisitions or by a longer TR. The two mentioned techniques are more suitable for imaging the tissue structures (which can be considered as spatially and temporally stable), and the resulting images being called *structural MRI (sMRI)*, rather than imaging a dynamic effect (as *functional responses*, which will be covered in Section 1.2). *Functional responses* are mostly imaged using *echo-planar imaging* [2,3] where image acquisition times of less than 40 ms for each image are achieved with the price of reduced resolution (but still it has superior resolution to magneto-encephalography (MEG), positron emission tomography (PET) and electro-encephalography (EEG)).

1.2 Functional Magnetic Resonance Imaging

In this section we will have a short review of how *functional magnetic resonance imaging*, and particulary *blood-oxygen-level dependent* (BOLD) contrast imaging, is done, what the limitations are and what processing steps are typically applied to them. One should note that although other techniques can be used to perform fMRI, but echo planar imaging (EPI), and more generally single-shot one-rf pulse-per-image techniques are the most common and successful and our discussion will mostly consider EPI imaging.

1.2.1 Principles

Some of the most common physiological information which can be mapped using fMRI are [4]:

1. base-line cerebral blood volume [5, 6]
2. changes in blood volume [7, 8]
3. quantitative measures of baseline and changes in cerebral perfusion [9]
4. changes in blood oxygenation [10–14]
5. resting state oxygen extraction fraction [15]
6. changes in cerebral blood oxygen consumption ($CMRO_2$) [16, 17]

Deoxyhemoglobin (deoxy-Hb) is paramagnetic relative to the rest of the brain tissues and water, and oxyhemoglobin (oxy-Hb) has the same susceptibility as brain tissues and water, thus presence of dexoy-Hb will result in magnetic field distortions when placed in a magnetic field whereas oxy-Hb will not. Furthermore, water molecules precess at a frequency that is directly proportional to the magnetic field that they are experiencing and if the spins are precessing at different frequencies, they rapidly become out of phase and destructive addition of the spins results in no MRI signal. During the resting state, due to microscopic field distortions caused by deoxy-Hb molecules, MRI signal is attenuated compared to a stage where no deoxy-Hb molecules would be present. During activation, increase of blood flow results in a decrease of dexoy-HB molecules and therefore magnitude of the magnetic field distortions decreases leading to an increase in spin coherency and finally increase of MRI signal; This process is shown in Fig. 1.2 [4].

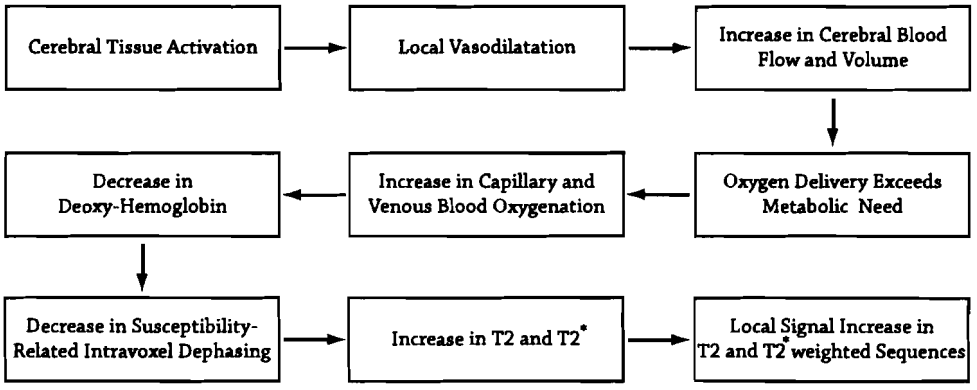

Figure 1.2: Stages of neuronal, physiological and biophysical relationships connecting neuronal activity to measured signal changes in fMRI.

1.2.2 Limitations

The accuracy of fMRI in mapping the brain activation is limited by two factors [4]: 1)the method by which the functional images are acquired and 2)the relationship between neural activity and the hemodynamic changes. In this section we will discuss the temporal, spatial and interpretative limits of fMRI.

Temporal Resolution

The total time per plane for single-shot EPI time-series collection is about 65 ms allowing for about 15 images to be collected in a second. Therefore, for a typical volume consisting of 30 slices a TR of 2 seconds is required. The hemodynamic response behaves like a low-pass filter with a latency of about 4 seconds (at stimuli on-off rates of 6 seconds, BOLD response starts to attenuate and at the rate of 2 seconds it is almost completely attenuated). Although the hemodynamics response attenuates the fast responses, it has been shown that activities with duration as low as 16 ms results in robust BOLD signal changes [4]. In principle, the hemodynamics response together with the readout window duration of the current imaging techniques largely affect precise temporal mapping of brain activities. Please refer to [4] and the references within for a more conclusive discussion of this topic.

Spatial Resolution

While recently developed techniques allow functional image resolution of about $1mm^3$ [18], the upper in-plane resolution of standard single-shot EPI is about $2mm^2$. As with the

temporal resolution, the spatial resolution is not only limited by the imaging techniques but also the underlying spatial spread of oxygenation changes that accompany focal brain activation [19]. The *hemodynamic point spread function* has been empirically determined to be on the order of $3mm^3$ [20]. Although limited solutions have been proposed to overcome these limitations leading to sub $1mm^3$ delineations [21,22], the ongoing question is whether detailed activation maps are precisely registered with the underlying function.

Interpretation

As fMRI is based on hemodynamic changes resulting in signal changes, the accuracy of fMRI maps rely on how accurate is the relationship between hemodynamic change and the underlying neural activity. Several strategies have been proposed to quantify the exact relationship between neural activity and the associated hemodynamic-related fMRI signal changes, which includes [4]:

- animal models and the simultaneous use of other measures of neuronal activity as via multiunit electrodes [23, 24] or more precise measures of hemodynamic changes via optical imaging [25]
- parametric modulation of magnitude or timing of activation in humans with corresponding measurements of fMRI signal changes
- simultaneous measures of neuronal activity (via implanted electrode or EEG) and fMRI signal changes
- nonsimultaneous measures of neuronal activity (MEG,EEG) and fMRI signal changes [26]
- modeling of the hemodynamic response and comparing the fMRI signal changes to precise activation magnitude, timing or pharmacological manipulations.

1.2.3 Post-Processing

There are a number of post-processing steps that should be taken to prepare the raw functional images, especially BOLD contrast images, for statistical analysis which mainly includes (one should note that depending on the desired statistical inference, some of the following steps might be removed from the processing pipeline):

1. **slice timing corrections**: for correcting the differences in image acquisition time between slices usually accompanying EPI systems [27, 28] especially for long TRs. When slices are acquired in an interleaved manner, timing of 1^{st} and 2^{nd} slices can differ by as much as $\frac{TR}{2}$. This process usually consists of re-sampling (filtering) the slices.

2. **re-alignment of time-series and unwrapping**: for removing movement artifacts, re-aligning the time-series fMRI volumes acquired from the same subject and compensating the nonhomogeneity of EPI imaging systems [29–33]. As it has been shown that some of these algorithms can cause spurious brain activations in the absence of subject motion [34], realignment and motion-correction algorithms should be used either when the subjects are prone to unwanted motion during scan time [35] or by cautious monitoring of the results.

3. **odd-even slice intensity correction**: for removing the *Nyquist ghost* artifacts caused by contiguous interleaved acquisition of the slices. This process is often called *Debanding* and consists of computing a constant, α, and applying intensity scalings of $(1-\alpha)$ and $(1+\alpha)$ to the odd and even slices respectively such that it minimizes an error criteria, usually the variance of voxel intensities over time.

4. **smoothing and intensity adjustment**: for reducing the noise, hopefully without significantly changing the over-all activation pattern of the functional images [36,37]. Note that spatial smoothing can result in some other beneficial effects too [38] which are not in the context of this work. The mean intensity level of each volume can also be adjusted to help reduce the effect of global changes in intensity over the scan time [39].

5. **co-registration**: for registering the functional image to the corresponding structural image of a subject the co-registration term is often used and it mostly involves simple rigid transformation and re-sampling of the functional image. Normalization is mostly referred to transforming image volumes of multiple subject to the same template space and is covered in Section 1.2.4. A rather complete survey of the existing co-registration and normalization methods can be found in [40].

1.2.4 Normalization

As was discussed in the previous sections, the recent developments in the physiological imaging modalities -positron emission tomography (PET) and functional MRI- have allowed for imaging studies aiming to localize human function in the brain. These studies involve a large number of subjects and one of the most important steps involved in statistical analysis of population studies is transforming each individuals' brain, or a specific region of interest (ROI), into a standard coordinate space. These normalizing transformations are designed to remove inter-subject morphological differences to aid in appropriate interpretation of functional signals in common coordinates.

Considering that fMRI and PET images have coarse resolutions and the functional patterns are not necessarily the same for all the subjects, they are not suitable for accurate normalization techniques, thus intrinsic study of brain functions will be based on the assumption that normalization techniques are able to establish the link between physiological responses and the high resolution structural images [41, 42]. The idea of using structural information in registering the physiological data was first suggested in [43] for PET images.

Current normalization approaches can be categorized into three major groups, voxel similarity, surface similarity and landmark based. Landmark based approaches often require manual human interference which can be susceptible to inter-rater variability and drift, while voxel and surface based approaches are better candidates for automatic normalization algorithms. Various automatic surface based normalization methods have been developed which mainly consist of two approaches:

- Flattening two cortical surfaces to a plane [44] or to a sphere [45] using variational methods or mechanical models and analyzing the data in the common flattened space [46].
- Working in the surface geometry itself rather than planes or sphere geometries by constructing metric distances between the corresponding points [47, 48]. Note that some of these approaches use manual delineated sulcal landmarks [48] to establish the correspondence.

Therefore, as most of the surface based approaches are constrained to the cortical region or require manual landmarks, they are not suitable for automatic analysis of large data-sets studying both sub-cortical and cortical areas.

Voxel similarity based normalization techniques can be divided into two major groups, affine (linear) or non-linear (small, large deformation) approaches. In the former all the voxels in a ROI go through the same transformation, while in the later each voxel can move in a different fashion although there is usually a smoothness constraint in the transformation of neighboring voxels. One of the most famous affine normalization techniques is the Talairach normalization procedure [49] where 12 rectangular regions of brain are mapped to the ones of the template brain using 12 parameter affine transformation. Some of the researchers compute the affine transformation of the whole-brain instead of computing a separate transformation for each individual rectangular volume. Widely used non-rigid small-deformation normalization technique implemented in statistical parameter mapping (SPM5) software package [50, 51] consists of first aligning the images using a 12 parameter affine registration and then using discrete cosine transformation (DCT) basis functions to warp the images into a standard coordinate space.

Viscous fluid approach [52] and large deformation mappings [53, 54] were developed to register the objects whose alignment require large deformations. From the same group of transformations, the large deformation diffeomorphic metric map (LDDMM) [55] uses the flow of velocity vector fields to construct the normalizing transformation and smoothness constraints on the velocity vector fields guarantee smooth and invertible diffeomorphic transformations. Under diffeomorphic transformation, connected sets remain connected, disjoint sets remain disjoint, smoothness of anatomical features is preserved and invertibility of transformation renders the choice of an anatomic template arbitrary. Since these methods do not take into account the variability of the cortical structure among subjects, the performance of these mappings can degrade in the cortex. In order to solve the performance degradation in cortical areas, as we will discuss in Section 1.3 and later on Chapter 2, our method consists of first aligning the brain segmentations (cortical/sub-cortical) using an affine transformation and then refining the mapping by computing the LDDMM transformation between the corresponding ROIs.

1.2.5 Statistical Analysis

Although many methods have been proposed for statistical analysis of functional MRI, they can be divided into two broad groups; intra-subject(single subject analysis) and inter-subject(group analysis):

1. **intra-subject statistical analysis**: The aim is to observe the functional patterns of the subject by assigning a value to each voxel based on time-series signal intensities of that voxel alone or in conjunction with other voxels. The simplest method is called the *substraction* method, where the mean of voxel intensities during the rest period is subtracted from the mean of voxel intensities during the task period and a simple student's t-test is applied to the whole brain to identify significant deviations from the baseline (zero activity). Although there are numerous intra-subject statistical analysis methods available to this date [56–58], fitting the data into a *general linear model* (GLM) [38, 59] and then performing t-tests or analysis of variance to generate statistical maps is the most commonly adapted method to perform intra-subject statistical analysis. Note that *contrast images* are not statistical maps but rather magnitude of the desired responses generated using the coefficients calculated while constructing the GLM.

2. **inter-subject statistical analysis**: Although most of the statistical analysis methods designed for intra-subject studies can be modified and applied to the inter-subject statistical analysis, the main difference between the two is the inter-subject variability of brain structures and the associated normalization problems (a good survey of existing methods can be found in [60]). The main contribution of this thesis is improving the inter-subject registration by combining a powerful segmentation tool, FreeSurfer [61], and a very powerful normalization method, large deformation diffeomorphic metric mapping (LDDMM) [55], in order to improve the normalization part of the functional MRI data analysis. This improvement tends to affect the later interpretation and the statistical results which will be seen in the next chapters.

Fixed versus random-effect analysis in group studies

If the goal of a functional imaging study involving many subjects is to draw statistical inferences regarding common effects occurring within that group which should be generalized to the population which the group was sampled from, the statistical analysis should be a *random effect analysis* [62]. In contrary to *random effect analysis*, *fixed effect analysis* can be used when the goal of the study is to only draw statistical inferences regarding the subjects involved in that study and not the population from which the subjects where sampled from. In the context of our work, *random effect analysis* translates into constructing

contrast images from each subject using GLMs, normalizing the resulting contrast images and performing voxel-wise statistical tests among corresponding voxels of the normalized contrast images [63, 64]. Furthermore, *fixed effect analysis* involves generating a single contrast image from all the subjects using a single multi-subject GLM and then performing statistical tests across the voxels of that image.

Statistical significance and the multiple measurements problem

The goal of any statistical test is identifying the voxels/regions which show significant deviation of the task signal from the baseline (control) signal. As was discussed previously, numerous methods exist to generate raw (un-thresholded) statistical maps and the obvious follow-up task will be to threshold these maps to identify the *statistically significant* voxels/regions. The inherit correlation between neighboring voxels in functional images imposes adapting multiple-measurement threshold correction approaches for identifying activated voxels/regions.

These approaches can generally be divided into the ones which set the activation thresholds based on individual voxel-wise test statistics [65] and the ones which threshold the activation maps based on the activity cluster size [66]. Controlling the false discovery rate (FDR) [67] has been shown to be more sensitive to local signal changes than the other common voxel-wise thresholing techniques (e.g. Bonferroni correction) and its rather easy implementation is well suited for functional data analysis. Bonferroni correction controls the chance of *any* false positives while FDR controls the *expected proportion* of the false positives. Bonferroni correction divides the desired significant level by the number of neighboring voxels (i.e. the number of voxels in the ROI) and finds the new threshold while FDR works by selecting a desired limit Q on FDR, ordering the p-values in the ROI, finding the largest i such that $p_i \leq \frac{i}{N} \times Q$ (where N is the total number of voxels in that ROI) and finally setting the new p-value threshold to p_i. It is worthwhile to note that as FDR is based on adaptively thresholding the p-values resulted from any statistical test by incorporating the number of voxels, unlike other thresholding methods which usually require adjusting the threshold throughout a study, a single FDR threshold can be used throughout a study regardless of the image volume size and the underlying statistical test.

1.3 Contributions of this Thesis

In group statistical analysis of functional MRI, localizing the statistically significant variations and the problem of multiple measurements associated with it, suggests the larger the search space the less sensitive the localizing method, i.e. if we study the whole brain it is more possible to miss the small details when compared to only studying a smaller ROI. Furthermore, it was shown in [68] that a better normalization will in fact increase the power of functional maps. These phenomena, together with the fact that normalization methods in general tend to perform better when the image volume is smaller, promise a more sensitive and better normalization for ROI-based functional MRI analysis. Moreover, although brain has a very complex anatomical structure (specially the cortical area), we are able to automatically segment it into well-defined anatomical regions [61, 69, 70]. It becomes intuitive to segment the (sub)cortical region into less complex segmentations, construct appropriate ROIs around these segmentations and perform accurate ROI-based statistical analysis after applying proper normalizations.

Our registration method is based on segmenting the cortical/sub-cortical area using the FreeSurfer software package [71, 72] into its constructing regions and normalizing the ROI around each segmentation independently based on LDDMM transformations. One should not that LDDMM had been previously used to normalize the functional images [68] but lack of an automatic accurate segmentation tool in the processing pipeline prevented conducting automated *bleeding* studies to quantify the normalization accuracy and identifying the sources of any functional patterns seen in a specific ROI by classifying it as *bleeding* from surrounding regions or *pure* functional signals originated from that ROI in each subject. It is of great interest to quantify the accuracy gained through using higher dimensional normalization techniques over lower less-complex ones and see if less accurate normalizations can lead to false activation maps. In short words, the contributions of this thesis are two-fold:

- We propose *bleeding* studies as not only a method of comparing the accuracy of normalization techniques but also as an effective approach for identifying the source of functional signals seen over the template space
- We propose a new ROI-based normalization pipeline aimed to increase the accuracy of brain functional maps

We hope the provided discussions will not only enable meaningful comparison of normalization techniques in the human brain mapping community but will also encourage the researchers to adapt our normalization pipeline in their future experiments.

In this thesis, in Chapter 2 we establish our ROI-based normalization method and compare its normalization accuracy with the two other previously mentioned normalization techniques by comparing the associated surface-to-surface distances together with a *bleeding* study conducted over a synthetic functional data-set. In Chapter 3 we apply our normalization technique to a real BOLD functional data-set and qualitatively compare the resulting statistical maps with both the *Affine* and *SPM5* normalization techniques; We will see how more accurate normalization techniques indeed increase the accuracy of the resulting functional brain maps and why the researchers in the brain mapping community should consider using the higher dimensional normalization techniques. Note that although Chapter 3 is mostly oriented around a BOLD functional data-set, as *LDDMM+FreeSurfer* is a normalization method independent of the underlying functional imaging modality, it will significantly improve the normalization results of any functional imaging study as well. We will finish this thesis in Chapter 4 by presenting the concluding marks and potential future works.

Chapter 2

Method

2.1 Introduction

As we previously discussed, the goal of this chapter is to formulate our normalization pipeline and compare the registration accuracy with the *Affine* and *SPM5* normalization methods by comparing the surface-to-surface distance profiles between the transformed FreeSurfer segmentations and the corresponding segmentation of the template and also conducting a *bleeding* study using a synthetic functional data-set. It is important to notice that normalization will be carried out using three different approaches:

1. **Affine transformation**: which is considered a linear transformation acting on the whole brain

2. **SPM5 transformation**: which is considered a low-dimensional non-linear transformation acting on the whole brain

3. **LDDMM+FreeSurfer transformation**: which is considered a high-dimensional non-linear transformation acting on a specific ROI

It is anticipated as the complexity of the spatial normalization method increases from *Affine* to *SPM5* and furthermore to *LDDMM+FreeSurfer*, the surface-to-surface distances become smaller and the associated bleedings become less at the expense of the increased computation complexity.

In [73] the performance of the *LDDMM+FreeSurfer* mapping approach, when applied to the cortex, was studied using synthesized fMRI data-sets based on *bleeding studies*. In this

chapter we are going to further evaluate the proposed normalization by not only studying a much larger data-set but also constructing isosurfaces from the (normalized) segmentations and quantifying the errors between the transformed segmentations and the corresponding segmentations of the template. Furthermore, in [73] the process of constructing the ROIs for the LDDMM normalization did not fully harness the segmentations provided by FreeSurfer and we will show that a simple segmentation-to-segmentation *Affine* alignment, before normalizing the corresponding ROIs, will greatly enhance the mapping accuracy.

In Section 2.2 we present the notations used in this chapter and then we will have a short review of *Affine*, *SPM5* and *LDDMM* normalization methods. In Section 2.3 we will describe how each normalization is computed, how *bleeding* study is conducted and how it is used to compare the accuracy of the mentioned normalization methods; We will also present surface-to-surface distances not only as a validation of our *bleeding* study but also as an additional accuracy measure. Section 2.4 contains the obtained *bleeding* results from our synthetic functional data-set as well as the associated surface-to-surface distance profiles. Conclusions of this chapter will be presented in Section 2.5.

2.2 The Normalization Techniques

2.2.1 Notation

Throughout this chapter the following notations will be used: $\Phi \circ \{.\}$ denotes transforming the $\{.\}$ using the transformation Φ, $\sum_{\mathcal{R}^3}$ is the sum over all the voxels in $\mathcal{R}^3$ and $\cup_{i=1}^{N_S}(.)$ is the union of $(.)$ in the $[1, N_S]$ range. S_i is the i^{th} subject, $S_i \in \Psi$ where Ψ is the set of all the subjects having N_S members and S_T is the template. $Seg_k^{S_i}$ is the k^{th} segmentation of the i^{th} subject provided by the FreeSurfer software package. $ROI_j^{S_i}$ is the j^{th} ROI of the i^{th} subject, referring to the j^{th} anatomical segmentation constrained in that region and $\mathfrak{ROI}$ is the set of all the $ROIs$. Although each anatomical region contains one or more segmentations, for simplicity, we assume that each anatomical region is constructed from a single segmentation. $Surf_j^{S_i}$ is the corresponding isosurface of $Seg_j^{S_i}$ generated by triangulation.

$\Phi_{S_i}^A$ and $\Phi_{S_i}^S$ are the *Affine* and *SPM5* transformations taking S_i to S_T. In the case of *Affine* and *SPM5* normalizations, ROI_j is the smallest possible rectangle containing $\cup_{i=1}^{N_S}(\Phi_{S_i}^A \circ Seg_j)$. $\Phi^A_{Seg_j^{S_i}}$ is the *Affine* transformation taking j^{th} segmentation of S_i to the

j^{th} segmentation of S_T. In the case of LDDMM normalizations, ROI_j is the smallest possible rectangle containing $\cup_{i=1}^{N_S}(\Phi^A_{Seg_j^{S_i}} \circ Seg_j)$. $\Phi^L_{ROI_j^{S_i}}$ is the LDDMM transformations taking j^{th} ROI of $\Phi^A_{Seg_j^{S_i}} \circ S_i$ to the j^{th} ROI of S_T.

2.2.2 Affine Normalization

Affine registration between each subject and the template was computed using an iterative, multi-resolution, multi-stage optimization approach. At each level, normalized mutual information was used as the distance criteria and the line-search optimization was adapted to minimize the cost function. The search space of the parameters for the *Affine* transformation was divided into four stages, 6 parameter rigid, 7 parameter iso-scale, 9 parameter uniso-scale and 12 parameter full *Affine* transformation; We will denote them as $\Phi^{A,6}$, $\Phi^{A,7}$, $\Phi^{A,9}$ and Φ^A respectively. We optimize the parameters at each stage using the initial-state parameters provided from the previous stage (except the first stage); Fig. 2.1 depicts the multi-stage nature of our *Affine* registration.

In other words, the *Affine* transformation is computed based on the following hierarchical equation set:

$$\begin{cases} \Phi^{A,6} &= \inf\limits_{\Phi^{A,6};\ \Phi_o^{A,6}=\mathbf{0}} \left\{ \frac{H(\Phi^{A,6}\circ S)+H(S_T)}{H(\Phi^{A,6}\circ S,S_T)} \right\} \\ \Phi^{A,7} &= \inf\limits_{\Phi^{A,7};\ \Phi_o^{A,7}=\Phi^{A,6}} \left\{ \frac{H(\Phi^{A,7}\circ S)+H(S_T)}{H(\Phi^{A,7}\circ S,S_T)} \right\} \\ \Phi^{A,9} &= \inf\limits_{\Phi^{A,9};\ \Phi_o^{A,9}=\Phi^{A,7}} \left\{ \frac{H(\Phi^{A,9}\circ S)+H(S_T)}{H(\Phi^{A,9}\circ S,S_T)} \right\} \\ \Phi^A_S &= \inf\limits_{\Phi^A;\ \Phi_o^A=\Phi^{A,9}} \left\{ \frac{H(\Phi^A\circ S)+H(S_T)}{H(\Phi^A\circ S,S_T)} \right\} \end{cases} \tag{2.1}$$

Where S is the subject, S_T is the template and $H(S)$ is the Shannon entropy of image S computed on the probability distribution of the gray level values. Furthermore, at each stage, 3 levels of resolution were incorporated to further avoid the local minimas. Note that at each level, subject and template were resampled into the same isotropic voxel resolution.

2.2.3 SPM5 Normalization

The normalization algorithm implemented in the *SPM5* software package [51] performs a two-step iterative search to find the transformation parameters. The first step of normalization is determining the optimum 12 parameter *Affine* transformation. Prior knowledge of the variability of head sizes is included within a Bayesian framework in order to increase

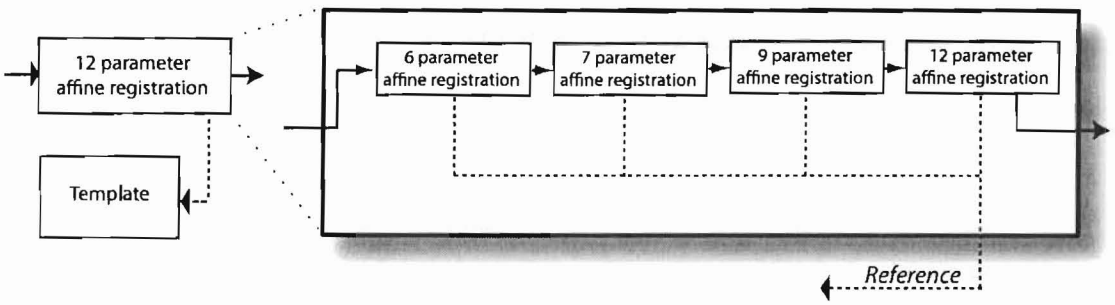

Figure 2.1: A closer look at the 12-parameter *Affine* transformation used throughout this thesis. The 12 parameter transformation can be divided into 4 stages: 6 parameter rigid followed by a 7 parameter iso-scale followed by a 9 parameter uniso-scale and finally a 12 parameter full *Affine* parameter estimation stage. Each stage provides the initial parameter values for the next stage.

the robustness and accuracy of the method. The second step is a non-linear normalization for correcting gross differences in head shapes that can not be accounted for by the *Affine* transformation alone. The non-linear warps are modeled by linear combination of smooth discrete cosine transformations bases functions (approximately 1000 lowest frequency ones). The coefficients of this bases function set are found by a maximum a posterior (MAP) parameter estimation.

The *Affine* parameter estimation is based on minimizing the sum of squared differences between target (S) and the template image (S_T). The non-linear spatial transformation from the $3D$ coordinate $\mathbf{x} = [x_1, x_2, x_3]$ at the target to the $3D$ coordinate $\mathbf{y} = [y_1, y_2, y_3]$ at the template can be formulated as:

$$\begin{cases} y_1 = x_1 + u_1 & = & x_1 + \sum_j q_{j1} d_j(\mathbf{x}) \\ y_2 = x_2 + u_2 & = & x_2 + \sum_j q_{j2} d_j(\mathbf{x}) \\ y_3 = x_3 + u_3 & = & x_3 + \sum_j q_{j3} d_j(\mathbf{x}) \end{cases} \tag{2.2}$$

Where q_{jk} is the j^{th} coefficient for dimension k and $d_j(x)$ is the j^{th} basis function at position $\mathbf{x}$. MAP parameter estimation finds the best set of q_{jk}'s based on the least-square Euclidean distance measure. Non-linear parameter search minimizes the sum of squared differences between the template and the target image while simultaneously minimizing the deviation of the transformation from its expected value. This technique requires the estimates of the likelihood of obtaining the fit given the data and accordingly prior knowledge of the spatial variability and also the knowledge of the variance associated with each voxel of the image.

As true variations associated with each voxel are not known, an empirical Bayesian method is used where the variations are estimated from the residual errors. The main assumption in this approach is the smoothness of both images which enables the method to use the correlation between neighboring voxels when estimating the variance. This assumption enforces smoothing images prior to registration which will accordingly reduce the accuracy of the computed transformation and can be seen as one of the major drawbacks of this approach.

2.2.4 LDDMM Normalization

The LDDMM algorithm [55] computes a transformation $\Phi^L : \Omega \rightarrow \Omega$ where $\Omega \subseteq \mathcal{R}^3$ is the $3D$ cube on which the data (structural and physiological) are defined. The transformation computed by LDDMM is the end point $\Phi^L = \phi_1$ of a flow of vector field $v_t \in V,\ t \in [0,1]$ given by the ordinary differential equation $\dot{\phi}_t = v_t(\phi_t)$, where ϕ_0 is identity $\phi_0(x) = x,\ x \in \Omega$. Enforcing smoothness on the vector fields $v \in V$ ensures that the solution to the differential equation $\dot{\phi}_t = v_t(\phi_t),\ t \in [0,1]$ is in the space of diffeomorphisms [74]. Smoothness is enforced by constraining the L^2 norm of several derivatives of the vector field to be in a Sobolev space with norm-square $||f||_V^2$ [55].

The optimal Φ^L is the minimum of the endpoint of the inexact matching problem

$$\inf_{\Phi^L=\phi_1} \int_0^1 ||v_t||_V^2 + \lambda D_{\Phi^L} \tag{2.3}$$

Where $\phi_1(x) = \int_0^1 ||v_t||_V^2 + \lambda D_{\Phi^L}$ and D_{Φ^L} is designed on the ROI or the MRI imagery and $\lambda > 0$ is the relative weight assignment. If S_T and S represent template and target images respectively, the transformation of the target image S under such transformation is a pull-back image defined by $\Phi^L \circ S = S \circ \Phi^{L^{-1}} = S(\Phi^{L^{-1}})$. If we denote the optimal transformation in the space of smooth velocity vector fields V on the domain Ω as $\hat{v}$, it can be formulated as:

$$\hat{v} = \underset{v:\dot{\phi}_t=v_t(\phi_t)}{\operatorname{argmin}} \left(\int_0^1 ||v_t||_V^2 dt + \frac{1}{\sigma_2} ||S \circ \phi_1^{-1} - S_T||_{L^2}^2 \right) \tag{2.4}$$

LDDMM algorithm is based on solving the above equation using an Euler-Lagrange estimation.

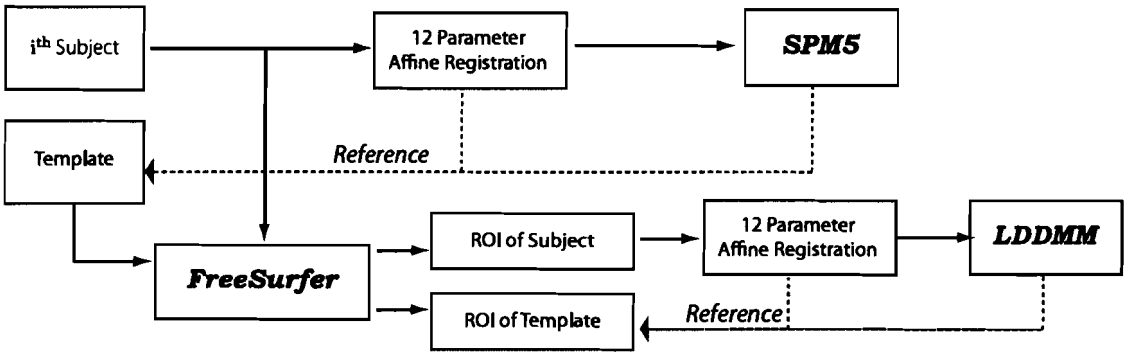

Figure 2.2: A simplified model of the processing pipeline. This processing pipeline presents two different normalization approaches: brain-to-brain normalization (*SPM5* and *Affine*) and ROI-to-ROI (*LDDMM+FreeSurfer*). FreeSurfer provides automatic segmentation of the brain to be further processed by the LDDMM normalization.

2.3 Quantification of the Normalization Methods

2.3.1 Model

Fig. 2.2 depicts a simplified model of the processing pipeline. In this processing pipeline, two different normalization approaches are present: the brain-to-brain normalization (*SPM5* and *Affine*) method and the ROI-to-ROI normalization (*LDDMM+FreeSurfer*) method. Although FreeSurfer segmentations are used to evaluate the performance of *SPM5* and *Affine* transformations, they are not incorporated in their normalization processes.

Affine Transformation

The first step of the processing pipeline is finding the 12 parameter *Affine* transformation, $\Phi^A_{S_i}$, taking $S_i : S_i \in \Psi$ to the template, S_T. The *Affine* transformations computed, $\Phi^A_{S_i}$, are applied to the corresponding segmentations and their respective *ROIs* of each subject. Therefore, $\Phi^A_{S_i} \circ S_i$, $\Phi^A_{S_i} \circ ROI_j^{S_i}$ and $\Phi^A_{S_i} \circ Seg_j^{S_i}$ will be the results of transforming the subjects' whole brain, the related *ROI* and the corresponding segmentations to the template space using the *Affine* transformation. The accuracy of the *Affine* transformation will be evaluated based on how close the transformed segmentations are to the templates' corresponding segmentation, i.e. how close $\Phi^A_{S_i} \circ Seg_j^{S_i}$ is to $Seg_j^{S_T}$.

Estimation		writing	
Parameter	*Value*	*Parameter*	*Value*
Template Image	S_T	Preserve	Concentrations
Template Weighting	None	Bounding Box	Cover All The Brain
Source Image	S_i	Voxel size	Same As Input
Source Smoothing	σ	Interpolation	Trilinear
Template Smoothing	σ	Wrapping	None
Affine Regularization	None		
Nonlinear Frequency Cutoff	25		
Nonlinear Iterations	16		
Nonlinear Regularization	1		

Table 2.1: SPM5 normalization parameters used throughout the course of this work.

SPM5 Transformation

SPM5 software package was used to compute the normalization, $\Phi^S_{S_i}$, taking $\Phi^A_{S_i} \circ S_i$ to the template, S_T. Table 2.3.1 shows the configuration used for the *SPM5* normalization. $\Phi^S_{S_i} \circ Seg_j^{S_i}$ and $\Phi^S_{S_i} \circ ROI_j^{S_i}$ are the related segmentation and the corresponding *ROI* of each subject transformed to the template space using the *SPM5* transformation. Same as above, $\Phi^S_{S_i} \circ Seg_j^{S_i}$ will be compared to $Seg_j^{S_T}$ in order to quantify the accuracy of the *SPM5* normalization.

LDDMM+FreeSurfer Transformation

The *Affine* transformation taking any segmentation of the subject, $Seg_j^{S_i}$, to the corresponding segmentation of the template, $Seg_j^{S_T}$, were computed and applied to the corresponding ROI of that subject, $ROI_j^{S_i}$. Finally, the LDDMM map which transforms $\Phi^A_{Seg_j^{S_i}} \circ ROI_j^{S_i}$ to $ROI_j^{S_T}$ was computed. Same as the two previous cases, the accuracy of the *LDDMM+FreeSurfer* method is determined by quantifying how well the transformed segmentation, $\Phi^L_{ROI_j^{S_I}} \circ (\Phi^A_{Seg_j^{S_i}} \circ Seg_j^{S_i})$, matches $Seg_j^{S_T}$.

2.3.2 Bleeding

In this section, we define the *bleeding* phenomena used to quantify the accuracy of a normalization method, we discuss how two types of *bleeding* can be constructed and we show that only one of them is relevant and is possible to be quantified. We also present the synthesized fMRI data-set generated for this study and how *bleeding* is calculated using this data-set.

Bleeding from inside a segmented structure to its surrounding regions and vice versa

Assume each and every subject have functional activity localized inside its j^{th} segmentation, the segmentation is perfect and no functional artifacts are present. Upon perfect normalization, there should be no observed activity outside the j^{th} segmentation of the template, i.e. no functional signal should *bleed* from inside the j^{th} segmentation of the template to the surrounding regions. Upon imperfect normalization, some of the signals associated with each subjects' j^{th} segmentation will be mapped to outside the templates' j^{th} segmentation. This effect can be called the *outward bleeding.*

The *inward bleeding* can be similarly defined as the amount of signal present inside the j^{th} segmentation of the template when all the subjects had functional signal only outside their corresponding j^{th} segmentation. However, there is a major flaw in the definition of the *inward bleeding*:
In the case of a normalization which does not bring the analogous segmentation of each subject to the same coordinate space, the functional activity localized outside each segmentation, will entirely map to the outside region of the corresponding segmentation in the template space, and inward bleeding will be zero.
Therefore, from this point on, the *bleeding* notion will only indicate bleeding from inside of each segmentation to its surrounding regions (*outward bleeding*) and not vice versa.

Synthesized fMRI data-set and quantification of *bleeding*

Quantification of the *bleeding* effect described above requires a controlled data-set where the only present variable is the inter-subject (and not the intra-subject) morphological variability. The only possible way of eliminating the unwanted variables is creating a synthesized functional data-set, where not only the fMR signal is generated in the same way for all the subjects but also the generated signal is evenly distributed for each subject. Our method of controlled fMR signal generation is based on smoothing the automatic black-and-white segmentations provided by FreeSurfer, $Seg_j^{S_i}$, using a gaussian kernel, G_σ. G_σ is designed considering the image properties such that the result of smoothing resembles functional activity covering both inside and peripheral areas of Seg_j.

For generating the synthesized functional activity localized inside the j^{th} segmentation of the i^{th} subject, we mask the corresponding smoothed segmentation with the segmentation

itself. This operation can be denoted by:

$$F_j^i = \left(G_\sigma * Seg_j^{S_i}\right) \cap Seg_j^{S_i} \quad \text{for any } i \text{ and } j \tag{2.5}$$

Where F_j^i is the synthesized functional activity for the i^{th} subject localized inside its j^{th} segmentation. Following the argument presented in Section 2.3.2, If we synthesize functional activity inside the cortical/subcortical segmentation of each subject and then transform all the subjects to the common template, a better normalization will be the one which results in less activity observed outside the corresponding cortical/subcortical segmentation in the template space, or in other words, the less erroneous functional activity found outside the corresponding regions of the template the better the normalization. Therefore, the normalized *bleeding* can be defined as sum of the intensity values of all the transformed synthesized functional data masked with the complement of the corresponding segmentation of the template, normalized by the sum of the intensity values of these transformed synthesized functional data:

$$Bleeding_{Seg_j} = \frac{\sum_i \sum_{\mathcal{R}^3} \left\{\left(\Phi_i \circ F_j^i\right) \cap comp(Seg_j^T)\right\}}{\sum_i \sum_{\mathcal{R}^3} \left\{\Phi_i \circ F_j^i\right\}} \tag{2.6}$$

Where Φ_i is the normalization computed through the *Affine*, *SPM5* or the LDDMM method and $comp(.)$ is defined as:

$$comp(A)|_{i,j,k} = \begin{cases} 0 & \text{if } A(i,j,k) > 0 \\ 1 & \text{if } A(i,j,k) = 0 \end{cases}$$

2.3.3 Surface-to-Surface Euclidean Distance Computation and Statistical Analysis of the Distance Profiles

We use isosurface generation to generate the triangulated graphs representing the cortical/subcortical surfaces from the FreeSurfer segmentations, Seg_j. The Gueziec and Hummel [75] algorithm is used to generate a tessellation of triangles for an isosurface of a given intensity: $Seg_j \xrightarrow{Triangulation} Surf_j$ where $Surf_j$ is the isosurface corresponding to the j^{th} *Seg*. Finally, a distance is calculated between each vertex on the template surface, $Surf_j^T$, and the generated isosurface of the normalized subject, $\Phi_i \circ Surf_j^{S_i}$, using the method presented in [76]. Upon computing the distances, we generate the cumulative distribution function (CDF) of the surface-to-surface distances and the better normalization will be the

one which its related CDF approaches unity faster, i.e. the isosurfaces of the transformed segmentations lie closer to the templates' matching isosurfaces. Moreover, random variable X, with CDF $F(x)$, is said to be stochastically larger than random variable Y with CDF H if $F(x) \leq H(x)$ for all x, with strict inequality for at least one x [77]; After constructing the CDF functions, we can also quantify which normalization method results in stochastically larger distance values.

The nonparametric Wilcoxon rank-sum test [77, 78], tests the null hypothesis that two random variables have the same median where the assumptions are independent samples and continues distribution function of the samples. The surface-to-surface distance values for a segmentation of a subject can be averaged to give a representative of how well that segmentation was registered to the templates' corresponding segmentations. These mean values can be considered as independent samples of the average distance function associated with the underlying normalization method when applied to that specific segmentation. Now we can use the Wilcoxon rank-sum test on these mean values and quantify how any two normalization methods are different, in the average sense, for any such segmentation.

2.4 Results and Discussions

The subjects set consists of 48 healthy adults and their healthy siblings plus 40 schizophrenia patients and their siblings (total 176 subjects). Structural images were acquired using a coronal MP-RAGE 3D T1-weighted sequence (TR = 10 ms, TE = 4 ms, $flip$ = 8° performed on the 1.5T Siemens VISION system (Erlangen, Germany); voxel size = 1 × 1 × 1.25mm). For details of the image acquisition see [79]. FreeSurfer was applied to all the subjects, $S_i \in \Psi$, and $Seg_j^{S_i}$ were extracted. 8 regions, 6 from the cortical region representing the most complex and 2 from the subcortical region representing the less anatomically complex areas of the brain, were selected to compare the methods. One should note that some of the anatomical regions consists of multiple segmentations provided by FreeSurfer; Table 2.4 denotes the selected regions and their constructing segmentations and they are depicted in Fig. 2.3.

The brain-to-brain *Affine* transformations followed by the *SPM5* transformations were computed for all the subjects and the same series of transformations were applied to the corresponding segmentations of each subject. In the case of the *LDDMM+FreeSurfer* normalization, the segmentation related to a specific anatomical region of all the subjects were

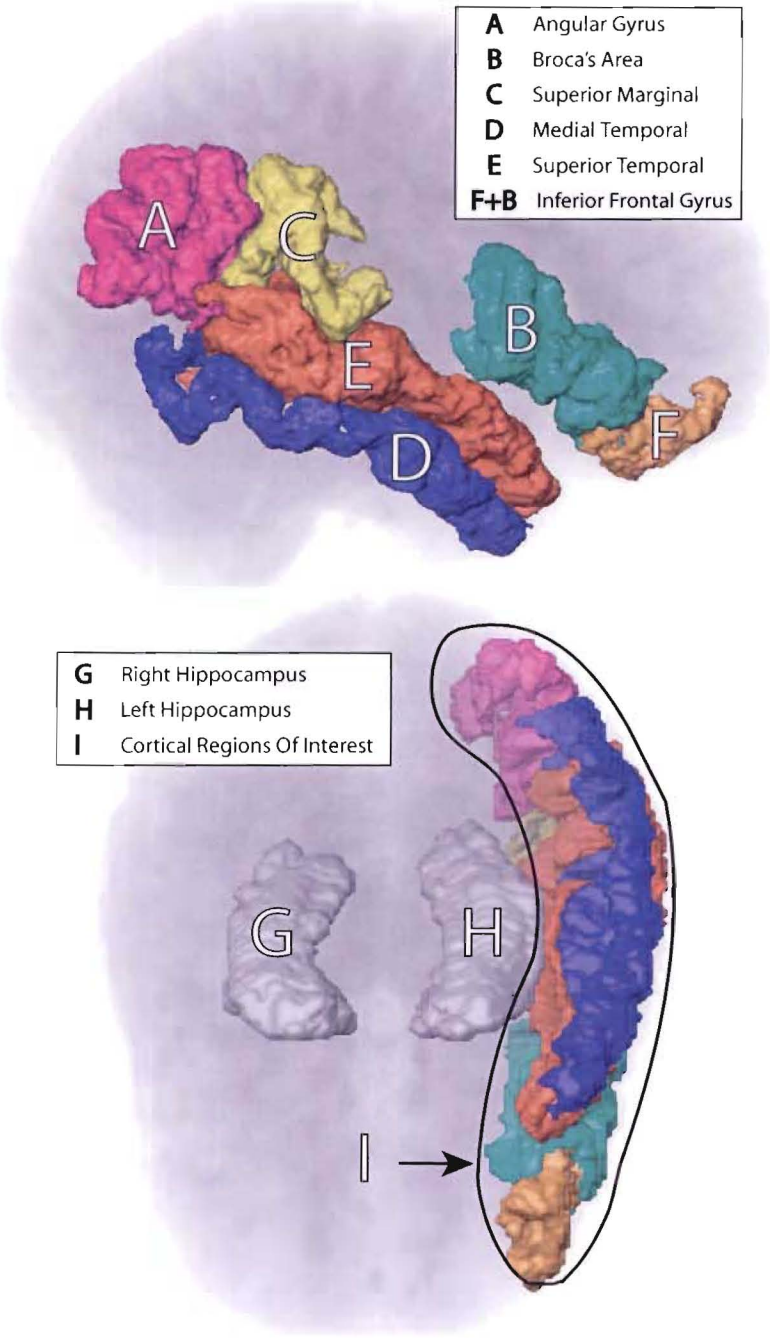

Figure 2.3: The cortical and subcortical anatomical regions selected for the comparison of the normalization methods.

ROI	Constructing Segmentations
Broca's Area	ctx-lh-(*parsopercularis* + *parstriangularis*)
Left Angular Gyrus	ctx-lh-*inferiorparietal*
Left Inferior Frontal Gyrus	ctx-lh-(*parsopercularis* + *parsorbitalis* + *parstriangularis*)
Left Medial Temporal Gyrus	ctx-lh-*middletemporal*
Left Supra Marginal Gyrus	ctx-lh-*supramarginal*
Left Superior Temporal Gyrus	ctx-lh-(*bankssts* + *superiortemporal* + *transversetemporal*)
Left Hippocampus	*left-hippocampus*
Right Hippocampus	*right-hippocampus*

Table 2.2: The anatomical regions and their constructing segmentations selected to compare the normalization methods as provided by FreeSurfer.

initially registered to the template using the segment-to-segment *Affine* transformation and then the LDDMM normalization was applied to the extracted ROIs. The bleeding study was performed based on the transformed segmentations and the results are shown in Fig. 2.4. It can be seen that in the simple-shaped regions, like hippocampus, *LDDMM+FreeSurfer* outperforms *SPM5* by 35% in average, and this number drops to 10% in the more complex cortical areas. Moreover, the *bleedings* associated with the *SPM5* and the *LDDMM+FreeSurfer* transformations show 0.093 and 0.070 standard deviation accordingly, which can lead to the observation that *SPM5* normalization has a wider accuracy spread over various brain regions when compared to *LDDMM+FreeSurfer.*

The CDF of the surface-to-surface distances were also computed and they are presented in Fig. 2.5. It can be seen that the mapping accuracy has a direct relationship with the amount of bleeding, i.e. the less bleeding means better normalization which also translates to the CDF associated with the method reaching unity faster. It also can be observed that whenever the gap between two CDF functions is bigger, the difference between the amounts of bleeding is also higher which again confirms the validity of the proposed comparison methods. From Fig. 2.5, it can be observed that the distance values of the *Affine* and *SPM5* normalized images are stochastically larger than the distance values of the corresponding *LDDMM+FreeSurfer* normalized images. The results of the statistical tests are also presented in Table 2.3 where it is shown that the null hypothesis that the average surface-to-surface distance values associated with the *SPM5* and *LDDMM+FreeSurfer* normalization methods have the same median can be rejected at 5% significant level. As the *Affine* registration is less accurate than the *SPM5* method, the *LDDMM+FreeSurfer* vs.

Segmented region	*Compared methods*	*P value*
Left Angular Gyrus	LDDMM+FreeSurfer vs. SPM5	$5.7171e-007$
Broca's Area	LDDMM+FreeSurfer vs. SPM5	$7.2958e-009$
Left Inferior Frontal Gyrus	LDDMM+FreeSurfer vs. SPM5	$1.9247e-007$
Left Medial Temporal Gyrus	LDDMM+FreeSurfer vs. SPM5	0.0253
Left Supra Marginal Gyrus	LDDMM+FreeSurfer vs. SPM5	0.0018
Left Superior Temporal Gyrus	LDDMM+FreeSurfer vs. SPM5	$4.3870e-008$
Left Hippocampus	LDDMM+FreeSurfer vs. SPM5	$1.5799e-049$
Right Hippocampus	LDDMM+FreeSurfer vs. SPM5	$3.6034e-046$

Table 2.3: Results of the Wilcoxon rank-sum test against the null-hypothesis that the average surface-to-surface distance values associated with the *SPM5* and *LDDMM+FreeSurfer* normalization methods have the same median.

Affine results are omitted from this table and can be directly concluded that the null hypothesis that the average surface-to-surface distance values associated with the *Affine* and *LDDMM+FreeSurfer* normalization methods have the same median can also be rejected at 5% significant level.

2.5 Chapter Summary

We proposed a new pipeline for automatically normalizing anatomical regions among large number of subjects using the LDDMM normalization method applied to the registered ROIs of the segmentations provided by the FreeSurfer software package. We compared our proposed method with the *Affine* normalization as well as the widely used small-deformation normalization technique implemented in the *SPM5* software package. We demonstrated the superiority of our method by conducting *bleeding* studies together with quantifying surface-to-surface distance profiles. Although always outperforming the other two methods, it was shown that the accuracy of the *LDDMM+FreeSurfer* normalization has an inverse relationship with the shape complexity of the underlying region and has a more robust performance in various anatomical areas when compared to the *SPM5* normalization method. Therefore, *LDDMM+FreeSurfer* was presented as a promising substitute for the *Affine* and *SPM5* normalization methods because of its higher robustness and registration accuracy.

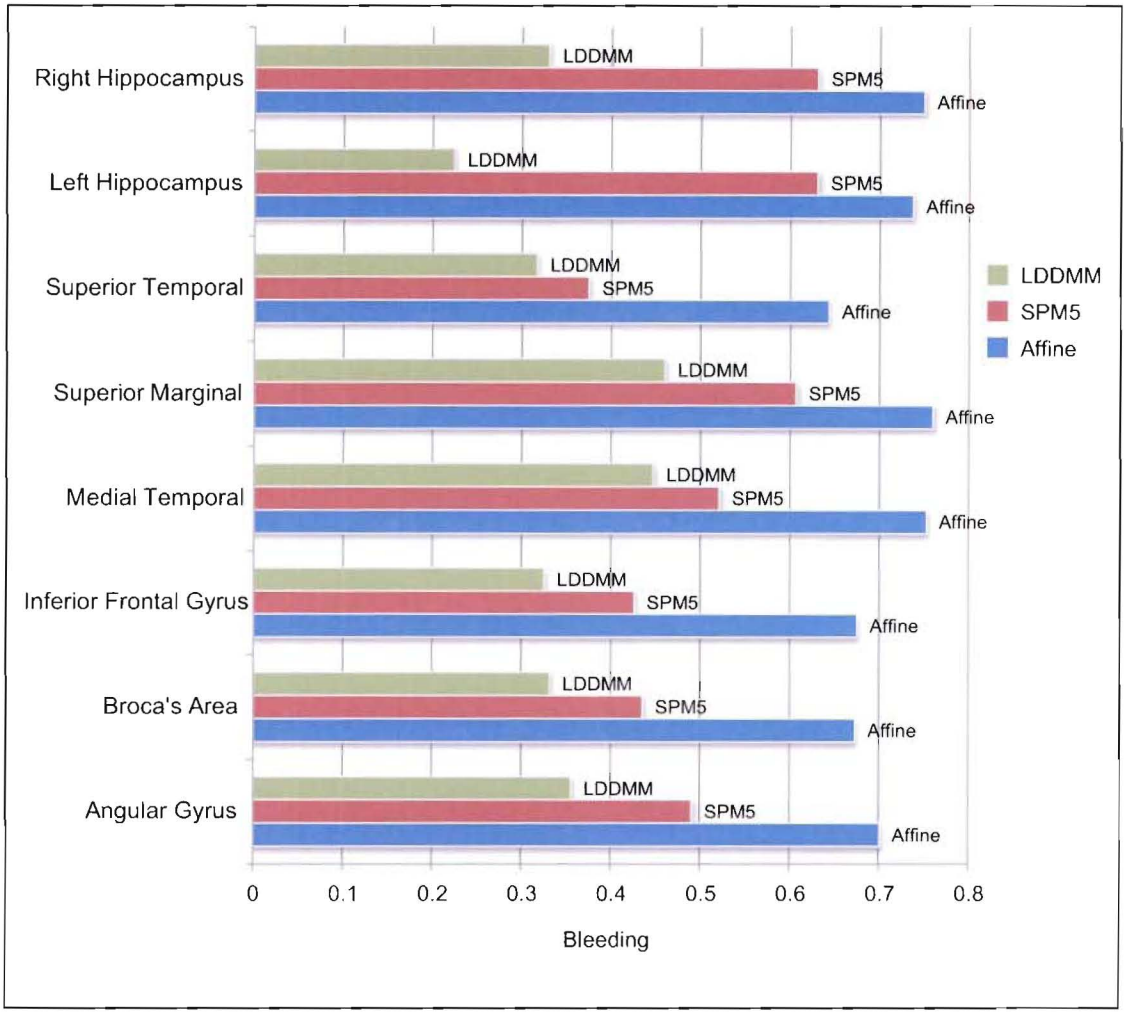

Figure 2.4: Bleedings from inside a region to its surrounding structures computed based on Eq. 2.6 for all the selected 8 ROIs. As the *Affine* transformation is computed based on minimizing the cost function over the whole brain, no region will have a better normalization then the other, and as can be seen, all the regions have almost the same amount of *bleeding*. It can be seen that the *SPM5* normalization has a better performance in the cortex than the subcortical regions and also the *bleedings* associated with the *LDDMM+FreeSurfer* normalization have an inverse relationship with the shape complexity of the underlying region, i.e. simple shaped regions, like hippocampus, have the least bleeding, while more complex shaped regions, like superior marginal gyrus, have the most bleeding.

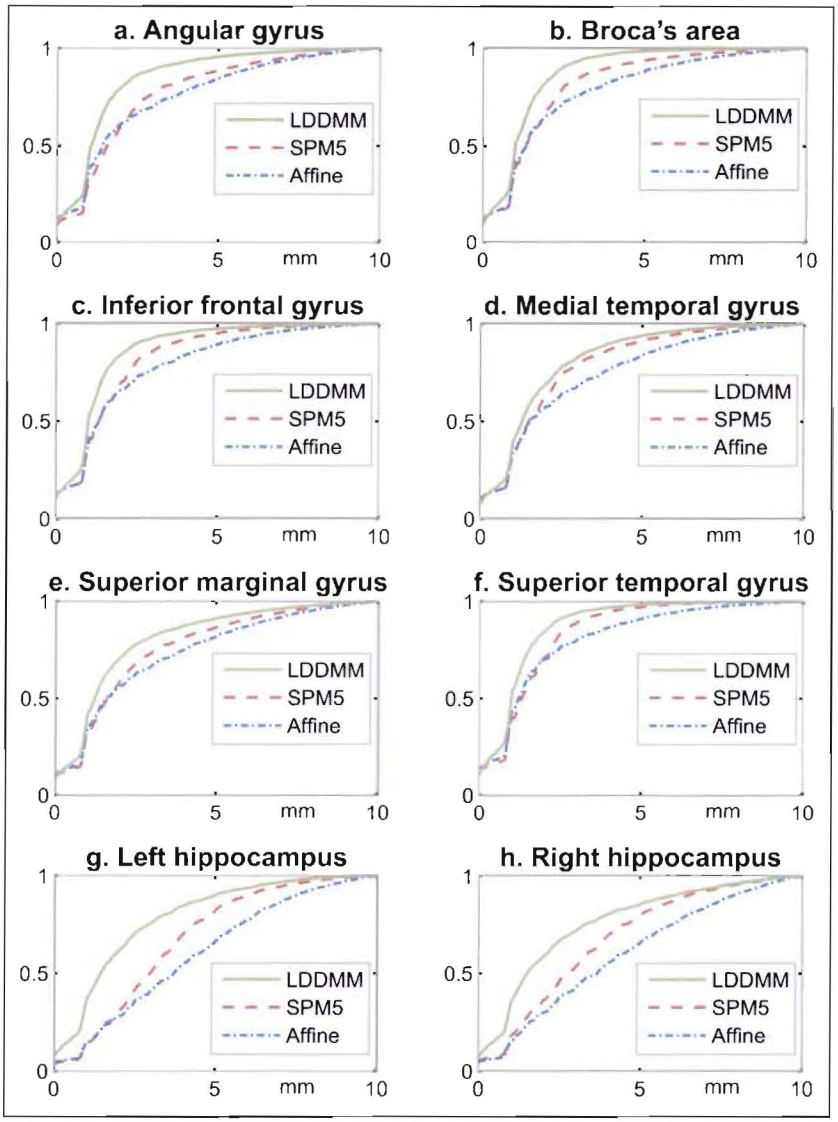

Figure 2.5: Cumulative distribution functions of the distance profiles from the triangulated $\Phi \circ Seg_j^{S_i}$ to the triangulated $Seg_j^{S_T}$ when using LDDMM(the green curve), *SPM5*(the red curve) and the *Affine*(the blue curve) transformations. The CDFs were computed for **a**-angular gyrus, **b**-Broca's area, **c**-inferior frontal gyrus, **d**-medial temporal, **e**-superior marginal, **f**-superior temporal, **g**-left hippocampus and **h**-right hippocampus regions. Besides the fact that the *LDDMM+FreeSurfer* normalization outperforms the two other methods, variability of the gap between the *LDDMM+FreeSurfer* normalization performance and the two other methods among different regions can be related to the varying complexity of the underlying regions, i.e. the simpler the anatomic complexity of a region, the larger the gap between the *LDDMM+FreeSurfer* performance and the two other methods.

Chapter 3

A Case Study Using Real Functional Data

3.1 Introduction

The previous chapter formulated our normalization pipeline and demonstrated the superiority of the *LDDMM+FreeSurfer* normalization method over the *Affine* and *SPM5* methods through quantifying surface-to-surface distances and conducting a *bleeding* study using a synthesized functional data-set. If the increase in normalization accuracy does not translate into an increase in the functional localization, there will be no point in adapting the new method. Therefore, the effect of our claimed superiority in normalization accuracy has to be evident in the resulting statistical maps of real functional data-sets, otherwise the merits of adapting our more complex and more computationally expensive method will be questionable. We have selected a real BOLD functional data-set from a schizophrenia study comparing patients and subjects in *word* and *face* recognition tasks to qualitatively observe the benefits of increasing the normalization power in producing more accurate statistical maps.

Moreover, discussions and the results of Chapter 2 suggested that all the three selected normalization methods (*Affine*, *SPM5* and *LDDMM+FreeSurfer*) have variable performances in cortical and subcortical regions while *LDDMM+FreeSurfer* was always outperforming the other two. It becomes of great interest to select regions from both cortical and subcortical regions as our regions of interest to compare the statistical maps of this

schizophrenia BOLD functional data-set: hippocampus and inferior frontal gyrus will be studied in this chapter. Hippocampus was selected not only as a representative of the sub-cortical structures but also for its known rule in memory and recognition tasks; Inferior frontal gyrus (IFG) was also not only selected as a representative of the cortical regions but also for the known rule of the Broca's area in word processing and recognition tasks; Furthermore, processing both left and right hemispheres will enable us to observe the laterality effects in *word* and *face* recognition tasks.

In Section 3.2 we will describe the fMRI design paradigm, image collection methods and the post-processing steps taken to prepare the data for statistical analysis. Section 3.3 contains the obtained results and the corresponding detailed discussions. Section 3.4 concludes this chapter by presenting a short summary.

3.2 Methods

In this section we describe the underlying functional study, image acquisition parameters, the post-processing steps applied to the functional images before statistical analysis and finally we address the multiple measurements problem and the approach adapted in this thesis.

3.2.1 Image Collection and the Design Paradigm

Functional image data in this study were taken from a previous study ([79]) where 32 subjects with schizophrenia and 41 healthy comparison subjects were scanned while performing three tasks, each with both verbal (words) and non-verbal (face) stimuli:

1. "2Back" version of the "NBack"
2. internal encoding
3. recognition

We focused on the recognition task where participants were asked whether a given item had been presented during 1 or 2. For details of the task design see [79].

All scanning was performed on the 1.5T Siemens VISION system (Erlangen, Germany); The functional images were acquired using an asymmetric spin-echo, EP sequence sensitive BOLD contrast (T2*; TR = 2.500ms, TE = 50ms, field of view = 24cm, $flip$ = 90°).

For each functional run, 102 sets of 16 contiguous axial images, 8 mm thick, were acquired parallel to the anteriorposterior commissure plane (3.75×3.75mm in plane resolution) which results in the final voxel size of $3.75 \times 3.75 \times 8mm$. Structural images were acquired using a coronal MP-RAGE 3D T1-weighted sequence ($TR = 10$ ms, $TE = 4$ ms, $flip = 8°$; voxel size $= 1 \times 1 \times 1.25$mm). For details of the image acquisition see [79].

3.2.2 Post-Processing

As the main discussion of this thesis is around spatial normalization and the subsequent statistical analysis, we will divide the post-processing steps into two parts: a)pre-normalization b)normalization and statistical analysis.

Pre-normalization

As it was described in Section 1.2.3, after functional image-reconstruction the following post-processing steps were applied to the fMRI data:

1. slice-time correction using a sync interpolation
2. even-odd slice intensity correction by applying the *Debanding* process
3. re-alignment of time-series using a 6-parameter transformation
4. intensity adjustment to a whole-brain value of 1000
5. spatial smoothing with an 8mm full-with-at-half-maximum Gaussian kernel
6. co-registration to each subjects' T1-weighted structural image followed by re-sampling to voxel size of $1 \times 1 \times 1.25$mm

For each subject, the magnitude of task-related activation in each voxel was estimated using a general linear model and boxcar task function convolved with a Boynton hemodynamic response function with separate estimates for *face* and *word* recognition tasks.

Normalization and statistical analysis

Structural images, and consequently the associated functional images, were normalized to the template coordinate space using the three methods described in chapters 2.2 and 2.3. The 12-parameter *Affine* transformations taking each subject to the template space based

on the method presented in Section 2.2.2 were computed and the *SPM5* transformations were computed using the parameters presented in Table 2.3.1. As discussed in Section 2.3.1, FreeSurfer segmentations were used to initially register corresponding areas of each subject to the template then the LDDMM transformation mapping the ROI around each subjects' registered area to the corresponding ROI of the template were calculated. Finally the calculated mappings were applied to the functional images of each subject. In order to observe the effect of increasing the accuracy of the normalization method on the final statistical maps, following the *bleeding* phenomena presented in Section 2.3.2, three sets of functional images were processed:

1. If we mask the functional images of each subject with a specific FreeSurfer segmentation of a region and transform such images from all subjects to the template, the resulting image represents the functional signals from that specific region transformed to the template space. This set will give us a measure of how much pure functional signal of a specific region is present in the corresponding region of the template space.

2. Following the above argument, if we apply the inverse-masks to the magnitude functional images of each subject, the transformed functional images to the template space, when we consider only that specific segmentation of the template image, will represent the amount of signal from the surrounding regions present in that region of the template space. This set will give us a measure of how much erroneous functional signal from the surrounding structures of a specific region has *bled* into that region in the template space. Note that this *inward bleeding* is being quantified as a complement of the previous data-set, otherwise, as it was discussed in Section 2.3.2, we can not draw any comprehensive conclusions by only considering this set.

3. Finally, if we consider all the signals from an ROI around a specific segmentation, the observed signals over that specific segmentation of the template image will represent the above two signal sets together.

If we call the specific segmentation X, the three functional sets were named *Only-X*, *Everything-But-X* and *ROI-X* respectively. Obviously, the less *Everything-But-X* activity and the more *Only-X* activity the better the transformation.

After normalization, voxel-wise two-tailed simple t-test comparing the activation against zero over the template space was calculated and finally false discovery rate (FDR) correction approach was adapted as the solution for the multiple measurements problem.

3.3 Results and Discussions

Subjects were divided into two groups: *Controls* and *Probands*; Where Controls were the healthy subjects and the Proband subjects were the schizophrenia patients. As IFG and hippocampus are the selected ROIs for this study, the functional data-set were divided into six parts:

- IFG:
    1. Whole ROI around IFG
    2. Only IFG
    3. Everything but IFG
- Hippocampus:
    1. Whole ROI around hippocampus
    2. Only hippocampus
    3. Everything but hippocampus

After performing voxel-wise two-tailed t-tests on each functional data-set, the resulting t-maps were thresholded using the $FDR = 0.05$ criteria. The values of voxels passing the $FDR = 0.05$ threshold were set to their original raw t-values to observe the activation/de-activation patterns in the thresholded volumes. The colormap was designed to show deactivation as blue and activation as red and as the t-values get larger the Hue of the colors increases. When no voxel values were present to perform the t-test, that voxel was assigned the green color. Furthermore, one should note that the FDR threshold of 0.05 adaptively translates into a corresponding p-value threshold for each individual volume. Fig. 3.1 and Fig. 3.2 depict the $FDR = 0.05$ thresholded statistical maps of the left and right hemisphere IFG volumes respectively; Fig. 3.3 and Fig. 3.4 depict the $FDR = 0.05$ thresholded statistical maps of the left and right hemisphere hippocampus volumes respectively.

Considering the results of the previous chapter on synthetic functional data, besides the *Whole-ROI* case, the results of the two other functional sets (*Only-X*, *Everything-But-X*) -although not directly visible from the FDR thresholded volumes for all the cases, especially the left hippocampus case- are as predicted:

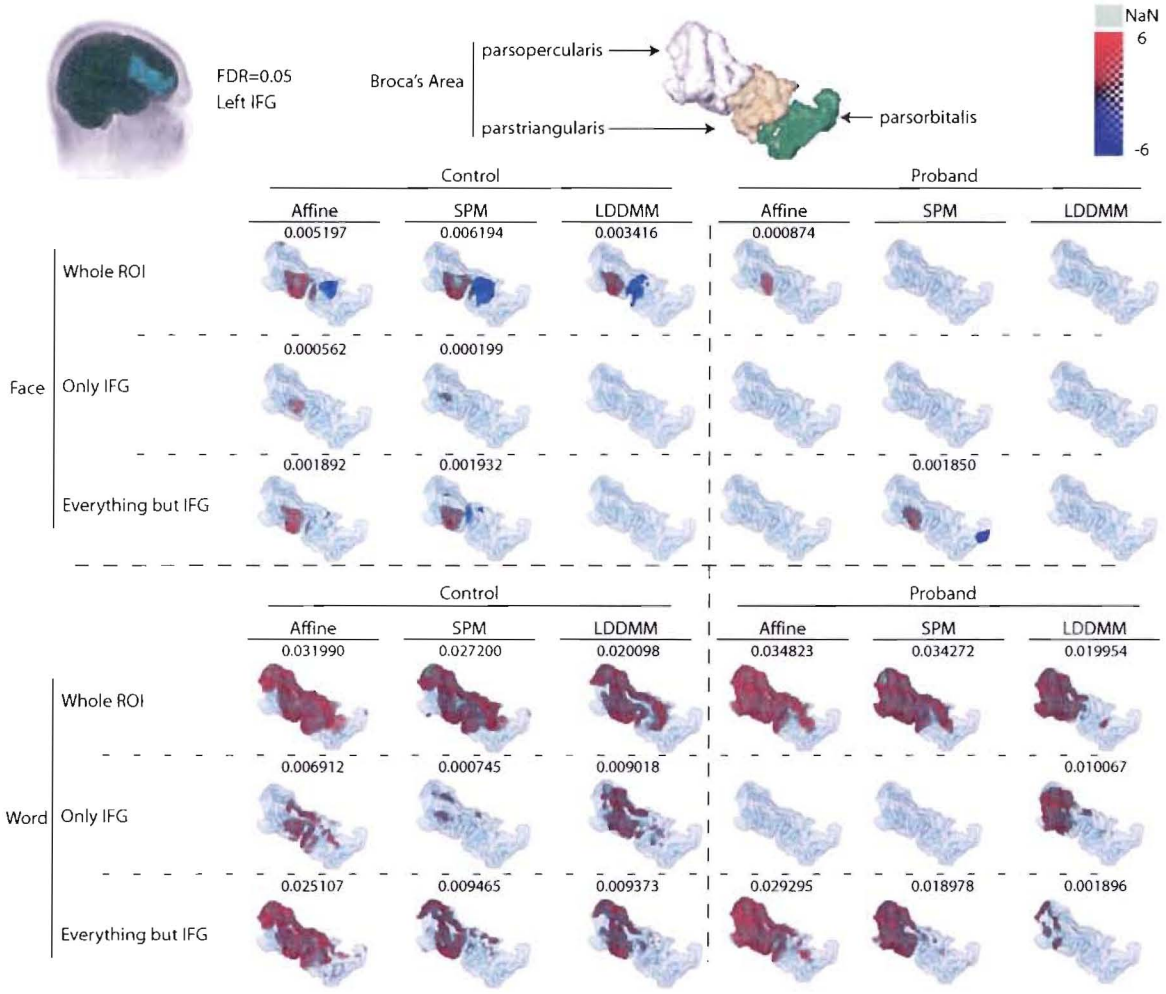

Figure 3.1: $FDR = 0.05$ thresholded statistical maps of the left hemisphere IFG volumes. Upper three rows show the *face* recognition results and lower three ones show the corresponding *word* recognition results. First three columns depict the results for the Control group and the next three columns are the results for the Proband group. Corresponding p-value thresholds (upon existence) are shown on top of each volume.

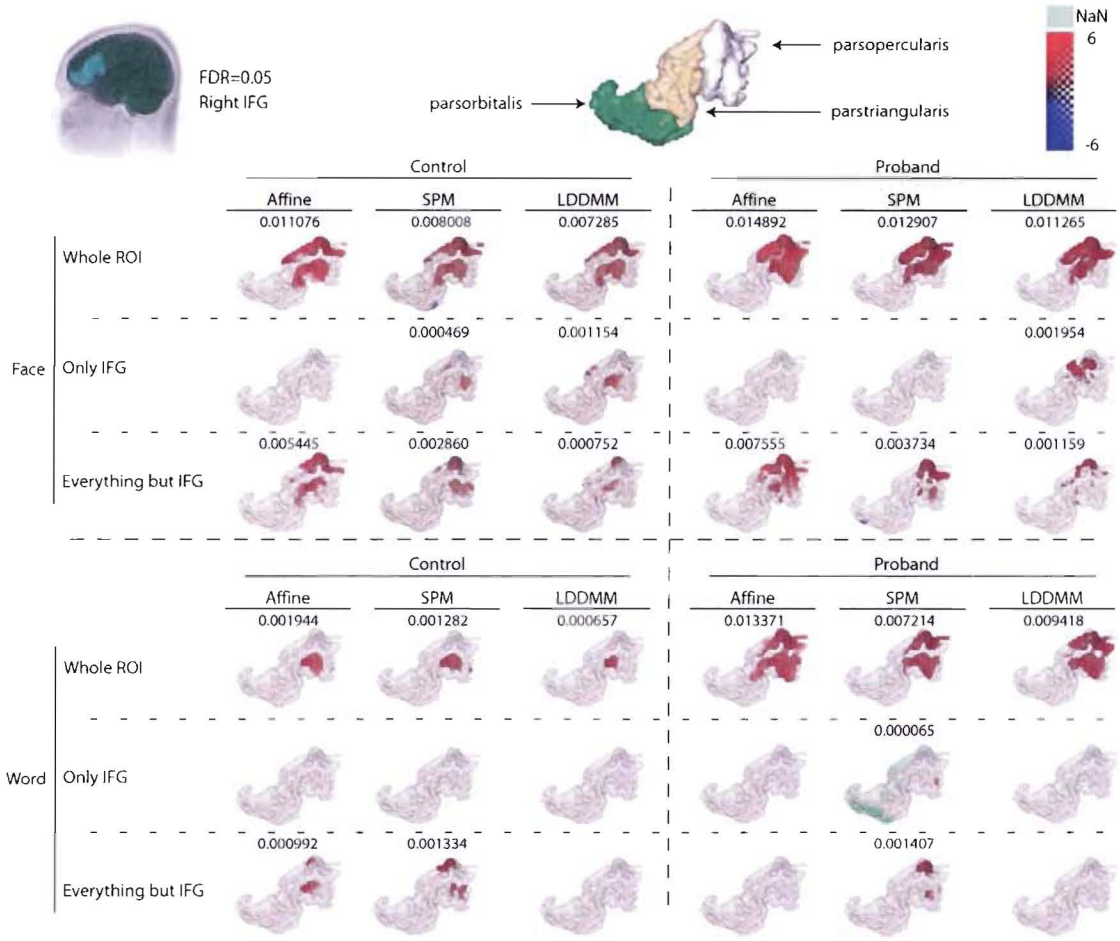

Figure 3.2: $FDR = 0.05$ thresholded statistical maps of the right hemisphere IFG volumes. Upper three rows show the *face* recognition results and lower three ones show the corresponding *word* recognition results. First three columns depict the results for the Control group and the next three columns are the results for the Proband group. Corresponding p-value thresholds (upon existence) are shown on top of each volume.

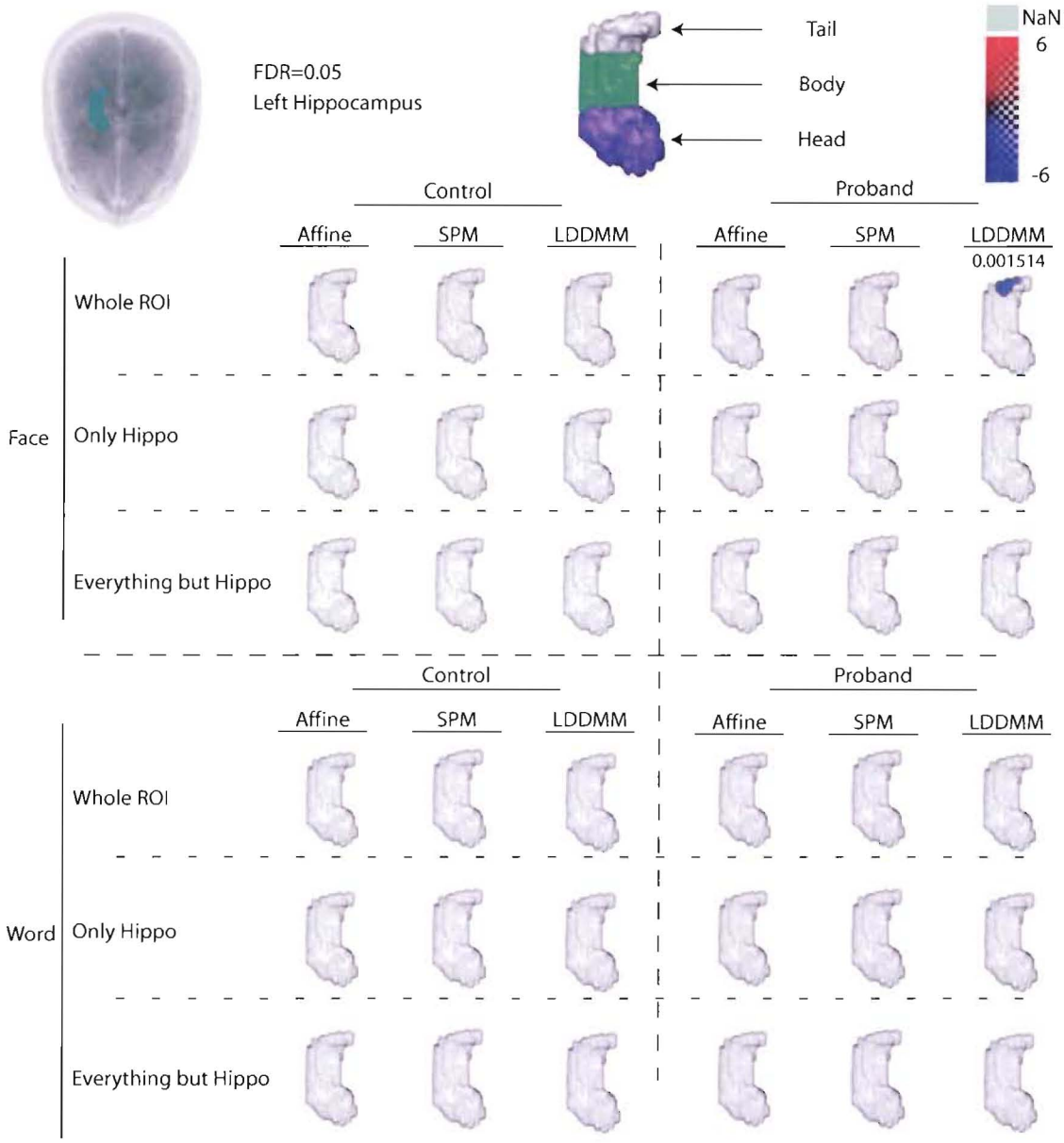

Figure 3.3: $FDR = 0.05$ thresholded statistical maps of the left hemisphere hippocampus volumes. Upper three rows show the *face* recognition results and lower three ones show the corresponding *word* recognition results. First three columns depict the results for the Control group and the next three columns are the results for the Proband group. Corresponding p-value thresholds (upon existence) are shown on top of each volume.

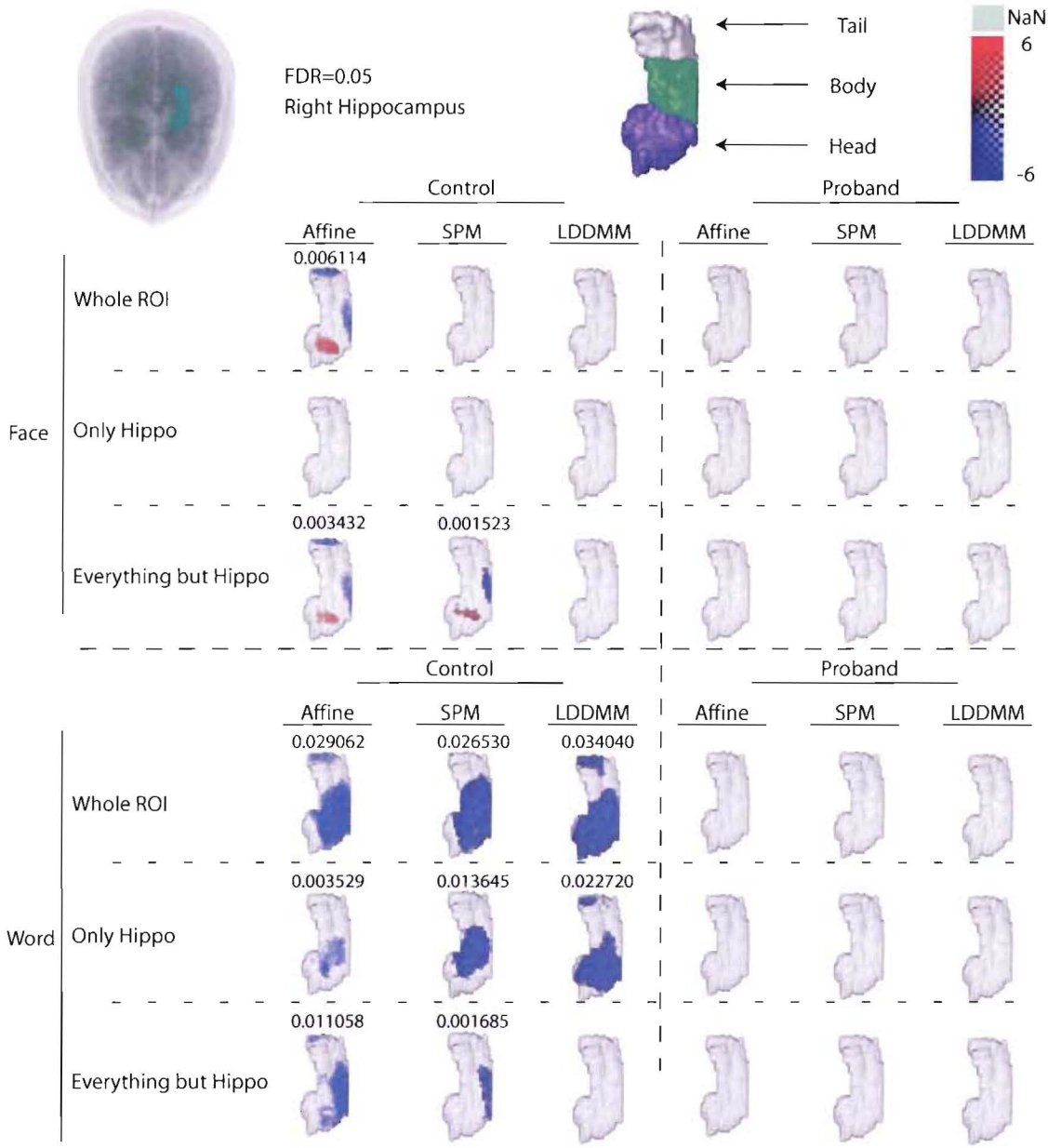

Figure 3.4: $FDR = 0.05$ thresholded statistical maps of the right hemisphere hippocampus volumes. Upper three rows show the *face* recognition results and lower three ones show the corresponding *word* recognition results. First three columns depict the results for the Control group and the next three columns are the results for the Proband group. Corresponding p-value thresholds (upon existence) are shown on top of each volume.

- **Only-X**: The *LDDMM+FreeSurfer* method has resulted in more voxels passing the FDR threshold compared to the *SPM5* method and the *SPM5* method itself has resulted in more voxels compared to the *Affine* approach. This observation agrees with the *bleeding* results from the previous chapter in the sense that if less signal is bleeding from inside a segmentation into its surrounding regions, we will have a better localization of functional signal over the template space.

- **Everything-But-X**: As one can predict, an inverse relationship between the accuracy of the underlying normalization method and the number of voxels passing the FDR threshold should hold here, i.e. the better the normalization the less erroneous signal from the surrounding regions should be present in any segmentation over the template space.

After the two above important observations, lets discuss how more accurate normalization has affected the statistical maps of the *Whole-ROI* volumes.

3.3.1 Inferior Frontal Gyrus Statistical Maps

The interesting observations can be summed up as follows:

- In the left IFG case for the *face-recognition* task in the Proband group (Fig. 3.1 first row, columns $4 \rightsquigarrow 6$), the *Affine* normalization method results in some activation over the *parsopercularis* area where no such pattern is visible in the output of *SPM5* and *LDDMM+FreeSurfer* methods.

- In the Left IFG case for the *word-recognition* task in the Control group (Fig. 3.1 forth row, columns $1 \rightsquigarrow 3$), both *Affine* and *SPM5* methods have resulted in some activation in the *parsorbitalis* area which is not preset in the *LDDMM+FreeSurfer* case. It should be noted that all the three methods show activation in the Borca's area which is the combination of *parsopercularis* and *parstriangularis* areas. As Broca's area is involved in speech processing, it was predicted that the Control group will show activation in this region.

- In the Left IFG case for the *word-recognition* task in the Proband group (Fig. 3.1 forth row, columns $4 \rightsquigarrow 6$), both *Affine* and *SPM5* methods have resulted in some activation in the *parstriangularis* and *parsorbitalis* areas which is not preset in the

results of the *LDDMM+FreeSurfer* method. Judging from the most accurate results, i.e. *LDDMM+FreeSurfer* results, schizophrenia patients fail to activate the left hemisphere *parsorbitalis* area compared to the Control group. It is worthwhile to notice that no such conclusion could be drawn using the *Affine* and *SPM5* normalization methods.

No such major difference can be seen in the right hemisphere IFG results and it can be associated with similar activation patterns of the right hemisphere IFG and its surrounding structures in this study where *bleedings* of the functional signal will not greatly affect the statistical maps compared to a situation where neighboring structures have different activation patterns.

3.3.2 Hippocampus Statistical Maps

The major differences between the three normalization method statistical maps can be pinpointed as follows:

- In the left hippocampus case for the *face-recognition* task in the Proband group (Fig. 3.3 first row, columns 4 $\rightsquigarrow$ 6), *LDDMM+FreeSurfer* method results in de-activation in the tail area while both *Affine* and *SPM5* methods fail to do so.

- In the right hippocampus case for the *face-recognition* task in the Control group (Fig. 3.4 first row, columns 1 $\rightsquigarrow$ 3), *Affine* method results in activation/de-activation in the all three parts of the hippocampus where the two more accurate normalization methods show no such activation/de-activation patterns. It is interesting to also look at the corresponding *Everything-But-Hippocampus* results where it's clearly shown that the observed activity for the *Affine* transformation in the *Whole-ROI* case is actually the *bleeding* from the surrounding regions into the hippocampus. Although the same *bleeding* pattern exists for the *SPM5* method too, the lower signal power of this bleeding prevents such activation/de-activation patterns to appear in the *Whole-ROI* case.

- In the right hippocampus case for the *word-recognition* task in the Control group (Fig. 3.4 forth row, columns 1 $\rightsquigarrow$ 3), all the three normalization methods show a de-activation pattern in the *head* and *body* areas. In addition, *LDDMM+FreeSurfer* have also resulted in a de-activated region in the *tail* area; Although *Affine* normalization

also shows this de-activated region in the *tail* area, the *Everything-But-Hippocampus* results suggest that this de-activated region is the result of the *bleedings* from its surrounding regions and it seems, by chance, this bleeding has resulted in a de-activated region which would be present from the hippocampus signal itself if one had used a more accurate normalization (e.g. *LDDMM+FreeSurfer*).

Although the $FDR = 0.05$ thresholded hippocampus volumes didn't clearly show the improvements gained through using more accurate normalization techniques, such observations can be made by analyzing the raw t-values. It should be noted that, by analyzing the raw t-values, although the observed effects will not generally quantify as statistically significant, but it will provide us with valuable information about how *bleeding* of functional signal in the normalization process can potentially affect the resulting statistical analysis.

Fig. 3.5 depicts the raw t-values of the left and right hemisphere hippocampal volumes for the *face* recognition task using the three normalization methods. Upper two and lower two rows show the left and right hippocampus results correspondingly. The most interesting phenomenon is the large activation region in the *head* area. This activated area seems to get smaller as the accuracy of the normalization method increases and it suggests that this activation might be caused by the *bleeding* from surrounding regions into the *head* area of the hippocampus and as more accurate normalization results in less bleeding, the associated activated region also gets smaller. As the closest region to the *head* area of the hippocampus is amygdala, in order to validate this theory, we have to see how much of the amygdala signal *bleeds* into the hippocampus as the result of inaccurate normalization.

For this purpose, we use the amygdala segmentations provided by FreeSurfer to mask the *Whole-ROI* functional volumes of hippocampus and then we apply the previously computed normalizations to them; The last step will be a two-tailed t-test over the hippocampus in the template coordinate space. In this way, we can see how much of the amygdala signal is *bleeding* into the hippocampus. Second and forth rows in Fig. 3.5 show the results of this concise bleeding study. As was predicted before, the activation pattern seen in the hippocampus is indeed the result of the amygdala signal *bleeding* into the hippocampus. Results of Chapter 2 suggest that the *Affine* and the *SPM5* methods have almost the same accuracy in the hippocampus area and it agrees with the results presented in Fig. 3.5 where the two methods have resulted in nearly the same amount of functional signal bleeding from amygdala into hippocampus while the *LDDMM+FreeSurfer* approach greatly outperforms them.

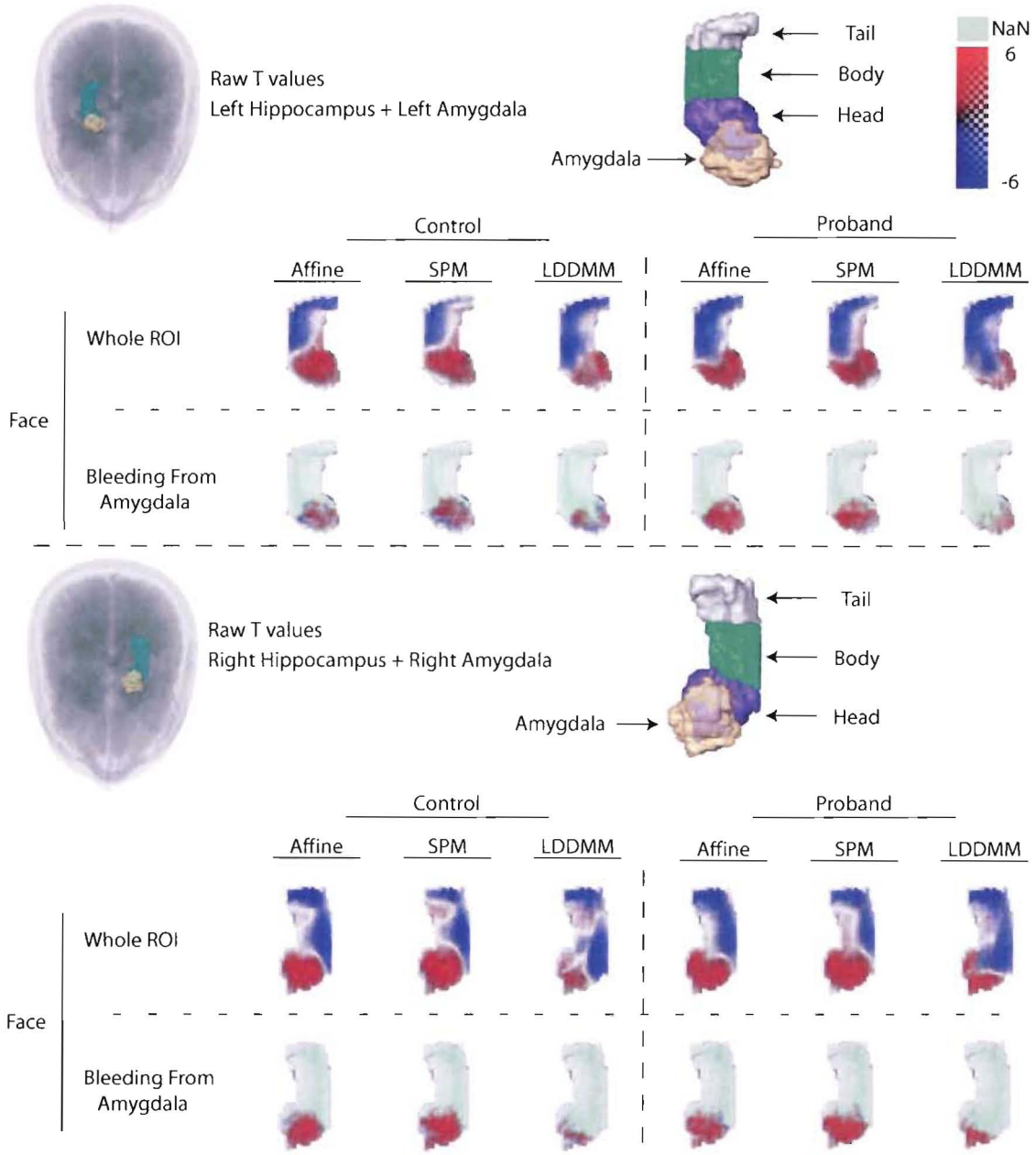

Figure 3.5: Raw t-value statistical maps of the right and left hemisphere hippocampal volumes. Upper two rows show the *face* recognition results for the left hippocampus and lower two ones show the corresponding *face* recognition results for the right hippocampus. First three columns depict the results for the Control group and the next three columns are the results for the Proband group. *Bleedings* from amygdala into hippocampus are shown in rows two and four. We can see how *bleeding* from amygdala into hippocampus gets smaller as the accuracy of the normalization method increases and how inaccurate normalization can potentially lead to false localization of activation in hippocampus.

3.4 Chapter Summary

We applied our ROI-based normalization method to a schizophrenia study real BOLD functional data-set and compared the resulting statistical maps with the ones obtained through using *Affine* and *SPM5* whole-brain-based normalization methods. We observed how less accurate normalization approaches can lead to inaccurate statistical maps and how *LDDMM+FreeSurfer* method can enhance this accuracy and enable group comparisons which would not be possible with the other two methods. Although statistically significant activation/de-activation differences are of the main interest in statistical analysis, we also showed that how inaccurate normalization can potentially affect the functional maps of the brain by quantifying the *bleedings* through analyzing the raw t-values.

Chapter 4

Conclusion

The main goal of this thesis was to propose a new fully automated ROI-based functional MRI normalization pipeline. This pipeline was composed of a high-dimensional non-linear registration method, *LDDMM*, and an automatic segmentation method, *FreeSurfer*. The superiority of this approach over two other commonly used whole-brain-based normalization approaches, *Affine* and *SPM5*, was shown through *bleeding* studies using synthesized functional volumes and surface-to-surface distance quantifications which demonstrated the higher structural normalization accuracy of *LDDMM+FreeSurfer* when compared to the other two methods. And finally, constructing statistical functional maps of a real BOLD functional data-set from a schizophrenia study by applying the transformations found from structural data to the corresponding functional data-set showed that significant improvements of the resulting brain functional maps can be gained through our normalization pipeline when compared to the other two methods. The above observation were made based on intra-group statistical analysis and it is predicted that such major differences will be present in the results of Control-vs-Proband or any other group statistical tests.

Although in Chapter 3 we studied the results of processing a real BOLD functional data-set, as *LDDMM+FreeSurfer* is a normalization method independent of the underlying functional imaging modality, the same improvements would happen if we had processed any other functional modality data-sets. However, as a result of lower resolution of other functional imaging modalities, e.g. PET and MEG, the increased accuracy in normalization of structural images gained through *LDDMM+FreeSurfer* might not result in the same amount of increase in localization of functional maps when compared to BOLD functional images. Nevertheless, *LDDMM+FreeSurfer* will always outperform the other normalization

methods thanks to its constructing components: high dimensional mapping and automatic segmentation of the brain structures.

As we stated before, *LDDMM* had been previously used to improve the accuracy of functional brain maps, but it relied on manual segmentations and no methods were present to study the source of observed functional patterns and whether they had been resulted from erroneous functional signals from neighboring structures or not. The incorporation of the *FreeSurfer* segmenting tool in the normalization pipeline enabled us to automatize the ROI-based mapping procedure and conduct *bleeding* studies not only to localize the source of functional signal maps seen over any regions of the template but also effectively compare brain normalization methods. Therefore, the *LDDMM+FreeSurfer* normalization method was shown to be suitable for accurate and automatic normalization of large functional MRI data-sets outperforming the *Affine* and the *SPM5* normalization approaches nominating it as a powerful substitute for them.

One should note that, in the normalization process, although we used the segmentations provided by *FreeSurfer* to align the corresponding structures of each subject to the template, they were not incorporated in computing the final mapping. Moreover, our proposed method was confined to ROI-based mapping and statistical analysis. Therefore, two potential future research subjects can be thought of:

- Modifying the *LDDMM* computation process so that it incorporates the extra information deductable from the corresponding structure surfaces which are available through *FreeSurfer*, e.g. which structures are neighbors and how the spatial relationship of their voxels should be preserved in the mapping process.

- Combining the ROI-to-ROI normalizations in order to build a brain-to-brain transformation for constructing the whole-brain functional map.

However, at this stage, the current whole-brain-based mappings such as the *Affine* and the *SPM5* methods can be used to provide the researchers with an initial (although potentially inaccurate) estimate of brain functional maps where they can flag the areas of interest which they would like to construct accurate functional maps through using *LDDMM+FreeSurfer*.

Bibliography

[1] D. Weishaupt, V. Köchli, and B. Marincek, *How Does Mri Work?: An Introduction to the Physics and Function of Magnetic Resonance Imaging.* Springer, 2003.

[2] F. Schmitt, M. Stehling, and R. Turner, *Echo-planar imaging: theory, technique and application.* Springer, 1998.

[3] M. K. Stehling, R. Turner, and P. Mansfield, "Echo-planar imaging: magnetic resonance imaging in a fraction of a second." *Science*, vol. 254, no. 5028, pp. 43–50, Oct 1991.

[4] J. D. Frank G. Hillary, *functional neuroimaging in clinical populations.* Guilford Press, 2007.

[5] B. R. Rosen, J. W. Belliveau, H. J. Aronen, D. Kennedy, B. R. Buchbinder, A. Fischman, M. Gruber, J. Glas, R. M. Weisskoff, and M. S. Cohen, "Susceptibility contrast imaging of cerebral blood volume: human experience." *Magn Reson Med*, vol. 22, no. 2, pp. 293–9; discussion 300–3, Dec 1991.

[6] B. R. Rosen, J. W. Belliveau, B. R. Buchbinder, R. C. McKinstry, L. M. Porkka, D. N. Kennedy, M. S. Neuder, C. R. Fisel, H. J. Aronen, and K. K. Kwong, "Contrast agents and cerebral hemodynamics." *Magn Reson Med*, vol. 19, no. 2, pp. 285–292, Jun 1991.

[7] J. Belliveau, D. Kennedy Jr, R. McKinstry, B. Buchbinder, R. Weisskoff, M. Cohen, J. Vevea, T. Brady, and B. Rosen, "Functional mapping of the human visual cortex by magnetic resonance imaging," *Science*, vol. 254, no. 5032, p. 716, 1991.

[8] H. Lu, X. Golay, J. J. Pekar, and P. C. M. V. Zijl, "Functional magnetic resonance imaging based on changes in vascular space occupancy." *Magn Reson Med*, vol. 50, no. 2, pp. 263–274, Aug 2003. [Online]. Available: http://dx.doi.org/10.1002/mrm.10519

[9] E. Wong, "Potential and pitfalls of arterial spin labeling based perfusion imaging techniques for mri," *Functional MRI. Heidelberg: Springer-Verlag*, pp. 63–69, 1999.

[10] S. Ogawa, D. W. Tank, R. Menon, J. M. Ellermann, S. G. Kim, H. Merkle, and K. Ugurbil, "Intrinsic signal changes accompanying sensory stimulation: functional brain mapping with magnetic resonance imaging." *Proc Natl Acad Sci U S A*, vol. 89, no. 13, pp. 5951–5955, Jul 1992.

[11] K. K. Kwong, J. W. Belliveau, D. A. Chesler, I. E. Goldberg, R. M. Weisskoff, B. P. Poncelet, D. N. Kennedy, B. E. Hoppel, M. S. Cohen, and R. Turner, "Dynamic magnetic resonance imaging of human brain activity during primary sensory stimulation." *Proc Natl Acad Sci U S A*, vol. 89, no. 12, pp. 5675–5679, Jun 1992.

[12] J. Frahm, H. Bruhn, K. D. Merboldt, and W. Hnicke, "Dynamic mr imaging of human brain oxygenation during rest and photic stimulation." *J Magn Reson Imaging*, vol. 2, no. 5, pp. 501–505, 1992.

[13] A. M. Blamire, S. Ogawa, K. Ugurbil, D. Rothman, G. McCarthy, J. M. Ellermann, F. Hyder, Z. Rattner, and R. G. Shulman, "Dynamic mapping of the human visual cortex by high-speed magnetic resonance imaging." *Proc Natl Acad Sci U S A*, vol. 89, no. 22, pp. 11 069–11 073, Nov 1992.

[14] P. A. Bandettini, E. C. Wong, R. S. Hinks, R. S. Tikofsky, and J. S. Hyde, "Time course epi of human brain function during task activation." *Magn Reson Med*, vol. 25, no. 2, pp. 390–397, Jun 1992.

[15] H. An, W. Lin, A. Celik, and Y. Z. Lee, "Quantitative measurements of cerebral metabolic rate of oxygen utilization using mri: a volunteer study." *NMR Biomed*, vol. 14, no. 7-8, pp. 441–447, 2001.

[16] T. L. Davis, K. K. Kwong, R. M. Weisskoff, and B. R. Rosen, "Calibrated functional mri: mapping the dynamics of oxidative metabolism." *Proc Natl Acad Sci U S A*, vol. 95, no. 4, pp. 1834–1839, Feb 1998.

[17] R. D. Hoge, J. Atkinson, B. Gill, G. R. Crelier, S. Marrett, and G. B. Pike, "Linear coupling between cerebral blood flow and oxygen consumption in activated human cortex." *Proc Natl Acad Sci U S A*, vol. 96, no. 16, pp. 9403–9408, Aug 1999.

[18] J. A. de Zwart, P. van Gelderen, P. Kellman, and J. H. Duyn, "Application of sensitivity-encoded echo-planar imaging for blood oxygen level-dependent functional brain imaging." *Magn Reson Med*, vol. 48, no. 6, pp. 1011–1020, Dec 2002. [Online]. Available: http://dx.doi.org/10.1002/mrm.10303

[19] L. M. Parkes, J. V. Schwarzbach, A. A. Bouts, R. H. R. Deckers, P. Pullens, C. M. Kerskens, and D. G. Norris, "Quantifying the spatial resolution of the gradient echo and spin echo bold response at 3 tesla." *Magn Reson Med*, vol. 54, no. 6, pp. 1465–1472, Dec 2005. [Online]. Available: http://dx.doi.org/10.1002/mrm.20712

[20] S. A. Engel, G. H. Glover, and B. A. Wandell, "Retinotopic organization in human visual cortex and the spatial precision of functional mri." *Cereb Cortex*, vol. 7, no. 2, pp. 181–192, Mar 1997.

[21] N. Logothetis, H. Merkle, M. Augath, T. Trinath, and K. Ugurbil, "Ultra high-resolution fmri in monkeys with implanted rf coils." *Neuron*, vol. 35, no. 2, pp. 227–242, Jul 2002.

[22] K. Cheng, R. A. Waggoner, and K. Tanaka, "Human ocular dominance columns as revealed by high-field functional magnetic resonance imaging." *Neuron*, vol. 32, no. 2, pp. 359–374, Oct 2001.

[23] C. Mathiesen, K. Caesar, N. Akgren, and M. Lauritzen, "Modification of activity-dependent increases of cerebral blood flow by excitatory synaptic activity and spikes in rat cerebellar cortex." *J Physiol*, vol. 512 (Pt 2), pp. 555–566, Oct 1998.

[24] N. K. Logothetis, J. Pauls, M. Augath, T. Trinath, and A. Oeltermann, "Neurophysiological investigation of the basis of the fmri signal." *Nature*, vol. 412, no. 6843, pp. 150–157, Jul 2001. [Online]. Available: http://dx.doi.org/10.1038/35084005

[25] A. J. Kennerley, J. Berwick, J. Martindale, D. Johnston, N. Papadakis, and J. E. Mayhew, "Concurrent fmri and optical measures for the investigation of the hemodynamic response function." *Magn Reson Med*, vol. 54, no. 2, pp. 354–365, Aug 2005. [Online]. Available: http://dx.doi.org/10.1002/mrm.20511

[26] H. Laufs, K. Krakow, P. Sterzer, E. Eger, A. Beyerle, A. Salek-Haddadi, and A. Kleinschmidt, "Electroencephalographic signatures of attentional and cognitive default modes in spontaneous brain activity fluctuations at rest." *Proc Natl Acad Sci U S A*, vol. 100, no. 19, pp. 11 053–11 058, Sep 2003. [Online]. Available: http://dx.doi.org/10.1073/pnas.1831638100

[27] S. J. Kiebel, S. Klppel, N. Weiskopf, and K. J. Friston, "Dynamic causal modeling: a generative model of slice timing in fmri." *Neuroimage*, vol. 34, no. 4, pp. 1487–1496, Feb 2007. [Online]. Available: http://dx.doi.org/10.1016/j.neuroimage.2006.10.026

[28] R. Henson, C. Buechel, O. Josephs, and K. Friston, "The slice-timing problem in event-related fmri," *Neuroimage*, vol. 9, no. 6 Pt 2, p. S125, 1999.

[29] L. Muresan, R. Renken, J. B. T. M. Roerdink, and H. Duifhuis, "Automated correction of spin-history related motion artefacts in fmri: simulated and phantom data." *IEEE Trans Biomed Eng*, vol. 52, no. 8, pp. 1450–1460, Aug 2005.

[30] K. Mathiak and S. Posse, "Evaluation of motion and realignment for functional magnetic resonance imaging in real time." *Magn Reson Med*, vol. 45, no. 1, pp. 167–171, Jan 2001.

[31] S. Grootoonk, C. Hutton, J. Ashburner, A. M. Howseman, O. Josephs, G. Rees, K. J. Friston, and R. Turner, "Characterization and correction of interpolation effects in the realignment of fmri time series." *Neuroimage*, vol. 11, no. 1, pp. 49–57, Jan 2000. [Online]. Available: http://dx.doi.org/10.1006/nimg.1999.0515

[32] R. W. Cox and A. Jesmanowicz, "Real-time 3d image registration for functional mri." *Magn Reson Med*, vol. 42, no. 6, pp. 1014–1018, Dec 1999.

[33] K. J. Friston, S. Williams, R. Howard, R. S. Frackowiak, and R. Turner, "Movement-related effects in fmri time-series." *Magn Reson Med*, vol. 35, no. 3, pp. 346–355, Mar 1996.

[34] L. Freire and J. F. Mangin, "Motion correction algorithms may create spurious brain activations in the absence of subject motion." *Neuroimage*, vol. 14, no. 3, pp. 709–722, Sep 2001. [Online]. Available: http://dx.doi.org/10.1006/nimg.2001.0869

[35] S.-S. Yoo, B.-G. Choi, R. Juh, C.-U. Pae, and C.-U. Lee, "Head motion analysis during cognitive fmri examination: application in patients with schizophrenia." *Neurosci Res*, vol. 53, no. 1, pp. 84–90, Sep 2005. [Online]. Available: http://dx.doi.org/10.1016/j.neures.2005.06.004

[36] K. J. Worsley and K. J. Friston, "Analysis of fmri time-series revisited–again." *Neuroimage*, vol. 2, no. 3, pp. 173–181, Sep 1995. [Online]. Available: http://dx.doi.org/10.1006/nimg.1995.1023

[37] C. Triantafyllou, R. D. Hoge, and L. L. Wald, "Effect of spatial smoothing on physiological noise in high-resolution fmri." *Neuroimage*, vol. 32, no. 2, pp. 551–557, Aug 2006. [Online]. Available: http://dx.doi.org/10.1016/j.neuroimage.2006.04.182

[38] R. Frackowiak, *Human Brain Function*, 2nd ed. Academic Press, 2004.

[39] P. M. Macey, K. E. Macey, R. Kumar, and R. M. Harper, "A method for removal of global effects from fmri time series." *Neuroimage*, vol. 22, no. 1, pp. 360–366, May 2004. [Online]. Available: http://dx.doi.org/10.1016/j.neuroimage.2003.12.042

[40] A. Gholipour, N. Kehtarnavaz, R. Briggs, M. Devous, and K. Gopinath, "Brain functional localization: a survey of image registration techniques." *IEEE Trans Med Imaging*, vol. 26, no. 4, pp. 427–451, Apr 2007.

[41] C. Maurer and J. Fitzpatrick, "A review of medical image registration," *Interactive Image-Guided Neurosurgery*, pp. 17–44, 1993.

[42] W. Wells and A. Jolesz, "Adaptive Segmentation of MRI Data," *Medical Imaging, IEEE Transactions on*, vol. 15, no. 4, p. 429, 1996.

[43] K. Friston, R. Passingham, J. Nutt, J. Heather, G. Sawle, and R. Frackowiak, "Localisation in PET images: direct fitting of the intercommissural (AC-PC) line." *J Cereb Blood Flow Metab*, vol. 9, no. 5, pp. 690–5, 1989.

[44] M. Hurdal, K. Stephenson, P. Bowers, D. Sumners, and D. Rottenberg, "Coordinate systems for conformal cerebellar flat maps," *NeuroImage*, vol. 11, 2000.

[45] B. Fischl, M. Sereno, R. Tootell, and A. Dale, "High-resolution intersubject averaging and a coordinate system for the cortical surface," *Human Brain Mapping*, vol. 8, no. 4, pp. 272–284, 1999.

[46] M. Bakircioglu, U. Grenander, N. Khaneja, and M. I. Miller, "Curve matching on brain surfaces using frenet distances." *Hum Brain Mapp*, vol. 6, no. 5-6, pp. 329–333, 1998.

[47] P. M. Thompson, R. P. Woods, M. S. Mega, and A. W. Toga, "Mathematical/computational challenges in creating deformable and probabilistic atlases of the human brain." *Hum Brain Mapp*, vol. 9, no. 2, pp. 81–92, Feb 2000.

[48] A. A. Joshi, D. W. Shattuck, P. M. Thompson, and R. M. Leahy, "A framework for registration, statistical characterization and classification of cortically constrained functional imaging data." *Inf Process Med Imaging*, vol. 19, pp. 186–196, 2005.

[49] J. Talairach and P. Tournoux, *Co-Planar Stereotaxic Atlas of the Human Brain: 3-Dimensional Proportional System: An Approach to Cerebral Imaging.* Thieme, 1988.

[50] K. Friston, J. Ashburner, C. Frith, J. Poline, J. Heather, and R. Frackowiak, "Spatial registration and normalization of images," *Human Brain Mapping*, vol. 2, no. 2, pp. 165–189, 1995.

[51] J. Ashburner and K. Friston, "The role of registration and spatial normalization in detecting activations in functional imaging," *Clinical MRI/Developments in MR*, vol. 7, pp. 26–28, 1997.

[52] G. E. Christensen, R. D. Rabbitt, and M. I. Miller, "Deformable templates using large deformation kinematics." *IEEE Trans Image Process*, vol. 5, no. 10, pp. 1435–1447, 1996. [Online]. Available: http://dx.doi.org/10.1109/83.536892

[53] J. Glaunès, M. Vaillant, and M. Miller, "Landmark matching via large deformation diffeomorphisms on the sphere," *Journal of Mathematical Imaging and Vision*, vol. 20, no. 1, pp. 179–200, 2004.

[54] B. Avants and J. Gee, "Shape averaging with diffeomorphic flows for atlas creation," *Biomedical Imaging: Macro to Nano, 2004. IEEE International Symposium on*, pp. 595–598, 2004.

[55] M. Beg, M. Miller, A. Trouvé, and L. Younes, "Computing Large Deformation Metric Mappings via Geodesic Flows of Diffeomorphisms," *International Journal of Computer Vision*, vol. 61, no. 2, pp. 139–157, 2005.

[56] K. Katanoda, Y. Matsuda, and M. Sugishita, "A spatio-temporal regression model for the analysis of functional mri data." *Neuroimage*, vol. 17, no. 3, pp. 1415–1428, Nov 2002.

[57] K. J. Worsley, C. H. Liao, J. Aston, V. Petre, G. H. Duncan, F. Morales, and A. C. Evans, "A general statistical analysis for fmri data." *Neuroimage*, vol. 15, no. 1, pp. 1–15, Jan 2002. [Online]. Available: http://dx.doi.org/10.1006/nimg.2001.0933

[58] G. Aguirre, P. Bandettini, and C. Moonen, *Functional MRI.* Springer New York, 1999.

[59] K. Friston, A. Holmes, K. Worsley, J. Poline, C. Frith, R. Frackowiak, *et al.*, "Statistical parametric maps in functional imaging: a general linear approach," *Human Brain Mapping*, vol. 2, no. 4, pp. 189–210, 1995.

[60] N. A. Lazar, B. Luna, J. A. Sweeney, and W. F. Eddy, "Combining brains: a survey of methods for statistical pooling of information." *Neuroimage*, vol. 16, no. 2, pp. 538–550, Jun 2002. [Online]. Available: http://dx.doi.org/10.1006/nimg.2002.1107

[61] G. Lohmann and D. von Cramon, "Automatic labelling of the human cortical surface using sulcal basins," *Medical Image Analysis*, vol. 4, no. 3, pp. 179–188, 2000.

[62] K. J. Friston, A. P. Holmes, C. J. Price, C. Bchel, and K. J. Worsley, "Multisubject fmri studies and conjunction analyses." *Neuroimage*, vol. 10, no. 4, pp. 385–396, Oct 1999. [Online]. Available: http://dx.doi.org/10.1006/nimg.1999.0484

[63] L. Frison and S. J. Pocock, "Repeated measures in clinical trials: analysis using mean summary statistics and its implications for design." *Stat Med*, vol. 11, no. 13, pp. 1685–1704, Sep 1992.

[64] K. J. Friston, K. E. Stephan, T. E. Lund, A. Morcom, and S. Kiebel, "Mixed-effects and fmri studies." *Neuroimage*, vol. 24, no. 1, pp. 244–252, Jan 2005. [Online]. Available: http://dx.doi.org/10.1016/j.neuroimage.2004.08.055

[65] B. R. Logan and D. B. Rowe, "An evaluation of thresholding techniques in fmri analysis." *Neuroimage*, vol. 22, no. 1, pp. 95–108, May 2004. [Online]. Available: http://dx.doi.org/10.1016/j.neuroimage.2003.12.047

[66] B. R. Logan, M. P. Geliazkova, and D. B. Rowe, "An evaluation of spatial thresholding techniques in fmri analysis." *Hum Brain Mapp*, Dec 2007. [Online]. Available: http://dx.doi.org/10.1002/hbm.20471

[67] C. R. Genovese, N. A. Lazar, and T. Nichols, "Thresholding of statistical maps in functional neuroimaging using the false discovery rate." *Neuroimage*, vol. 15, no. 4, pp. 870–878, Apr 2002. [Online]. Available: http://dx.doi.org/10.1006/nimg.2001.1037

[68] M. Miller, M. Beg, C. Ceritoglu, and C. Stark, "Increasing the power of functional maps of the medial temporal lobe by using large deformation diffeomorphic metric mapping," *Proceedings of the National Academy of Sciences*, vol. 102, no. 27, pp. 9685–9690, 2005.

[69] S. Sandor and R. Leahy, "Surface-based labeling of cortical anatomy using a deformable atlas," *Medical Imaging, IEEE Transactions on*, vol. 16, no. 1, pp. 41–54, 1997.

[70] C. Davatzikos and N. Bryan, "Using a deformable surface model to obtain a shape representationof the cortex," *Medical Imaging, IEEE Transactions on*, vol. 15, no. 6, pp. 785–795, 1996.

[71] B. Fischl, A. van der Kouwe, C. Destrieux, E. Halgren, F. Ségonne, D. Salat, E. Busa, L. Seidman, J. Goldstein, D. Kennedy, *et al.*, "Automatically Parcellating the Human Cerebral Cortex," *Cerebral Cortex*, vol. 14, pp. 11–22, 2004.

[72] R. Desikan, F. Segonne, B. Fischl, B. Quinn, B. Dickerson, D. Blacker, R. Buckner, A. Dale, R. Maguire, B. Hyman, *et al.*, "An automated labeling system for subdividing the human cerebral cortex on MRI scans into gyral based regions of interest." *Neuroimage*, 2006.

[73] B. Makouei, L. Wang, and M. Beg, "Enhanced Accuracy in Registration of Cortex Functional Data via Large-Deformation Differomorphic Maps," *Electrical and Computer Engineering, 2007. CCECE 2007. Canadian Conference on*, pp. 1159–1162, 2007.

[74] U. Grenander and M. Miller, "Computational anatomy: An emerging discipline," *Quarterly of Applied Mathematics*, vol. 56, no. 4, pp. 617–694, 1998.

[75] A. Gueziec and R. Hummel, "Exploiting triangulated surface extraction using tetrahedraldecomposition," *Visualization and Computer Graphics, IEEE Transactions on*, vol. 1, no. 4, pp. 328–342, 1995.

[76] J. Ratnanather, K. Botteron, T. Nishino, A. Massie, R. Lal, S. Patel, S. Peddi, R. Todd, and M. Miller, "Validating cortical surface analysis of medial prefrontal cortex," *NeuroImage*, vol. 14, no. 5, pp. 1058–1069, 2001.

[77] E. Lehmann, *Nonparametrics: Statistical Methods Based on Ranks, Revised.* Holden-Day, 1998.

[78] F. Wilcoxon, "Comparisons by ranking methods," *Biometric Bulletin*, vol. 1, pp. 80–82, 1945.

[79] D. M. Barch, J. G. Csernansky, T. Conturo, and A. Z. Snyder, "Working and long-term memory deficits in schizophrenia: is there a common prefrontal mechanism?" *J Abnorm Psychol*, vol. 111, no. 3, pp. 478–494, Aug 2002.

[80] A. Collignon, F. Maes, D. Delaere, D. Vandermeulen, P. Suetens, and G. Marchal, "Automated multi-modality image registration based on information theory," *Information Processing in Medical Imaging*, vol. 274, 1995.

[81] A. Collignon, D. Vandermeulen, P. Suetens, and G. Marchal, "3D Multi-Modality Medical Image Registration Using Feature Space Clustering," *Proceedings of the First International Conference on Computer Vision, Virtual Reality and Robotics in Medicine*, pp. 195–204, 1995.

[82] D. Collins, G. Le Goualher, and A. Evans, "Non-linear cerebral registration with sulcal constraints," *Proc. of Medical Image Computing and Computer-Assisted Intervention*, pp. 974–985, 1998.

[83] J. G. Csernansky, L. Wang, D. Jones, D. Rastogi-Cruz, J. A. Posener, G. Heydebrand, J. P. Miller, and M. I. Miller, "Hippocampal deformities in schizophrenia characterized by high dimensional brain mapping." *Am J Psychiatry*, vol. 159, no. 12, pp. 2000–2006, Dec 2002.

[84] J. G. Csernansky, L. Wang, S. C. Joshi, J. T. Ratnanather, and M. I. Miller, "Computational anatomy and neuropsychiatric disease: probabilistic assessment of variation and statistical inference of group difference, hemispheric asymmetry, and time-dependent change." *Neuroimage*, vol. 23 Suppl 1, pp. S56–S68, 2004. [Online]. Available: http://dx.doi.org/10.1016/j.neuroimage.2004.07.025

[85] R. Frackowiak, *Human Brain Function*, 2nd ed. Academic press, 2004, pp. 604–605.

[86] J. Haller, A. Banerjee, G. Christensen, M. Gado, S. Joshi, M. Miller, Y. Sheline, M. Vannier, and J. Csernansky, "3D hippocampalmorphometry by high dimensional transformation of a neuroanatomical atlas," *Radiology*, vol. 202, no. 2, pp. 504–510, 1997.

[87] D. Hill, C. Studholme, and D. Hawkes, "Voxel similarity measures for automated image registration," *Proceedings of SPIE*, vol. 2359, p. 205, 2003.

[88] F. Maes, A. Collignon, D. Vandermeulen, G. Marchal, and P. Suetens, "Multimodality image registration by maximization of mutualinformation," *Medical Imaging, IEEE Transactions on*, vol. 16, no. 2, pp. 187–198, 1997.

[89] H. Mann and D. Whitney, "On a Test of Whether one of Two Random Variables is Stochastically Larger than the Other," *The Annals of Mathematical Statistics*, vol. 18, no. 1, pp. 50–60, 1947.

[90] S. Ogawa, T. Lee, A. Nayak, and P. Glynn, "Oxygenation-sensitive contrast in magnetic resonance image of rodent brain at high magnetic fields." *Magn Reson Med*, vol. 14, no. 1, pp. 68–78, 1990.

[91] J. Pluim, J. Maintz, and M. Viergever, "Mutual-Information-Based Registration of Medical Images: A Survey," *IEEE TRANSACTIONS ON MEDICAL IMAGING*, vol. 22, no. 8, 2003.

[92] J. C. Pruessner, S. Khler, J. Crane, M. Pruessner, C. Lord, A. Byrne, N. Kabani, D. L. Collins, and A. C. Evans, "Volumetry of temporopolar, perirhinal, entorhinal and parahippocampal cortex from high-resolution mr images: considering the variability of the collateral sulcus." *Cereb Cortex*, vol. 12, no. 12, pp. 1342–1353, Dec 2002.

[93] U. E. Ruttimann, M. Unser, R. R. Rawlings, D. Rio, N. F. Ramsey, V. S. Mattay, D. W. Hommer, J. A. Frank, and D. R. Weinberger, "Statistical analysis of functional mri data in the wavelet domain." *IEEE Trans Med Imaging*, vol. 17, no. 2, pp. 142–154, Apr 1998.

[94] B. Thirion, P. Pinel, A. Tucholka, A. Roche, P. Ciuciu, J.-F. Mangin, and J.-B. Poline, "Structural analysis of fmri data revisited: improving the sensitivity and reliability of fmri group studies." *IEEE Trans Med Imaging*, vol. 26, no. 9, pp. 1256–1269, Sep 2007.

[95] D. Van Essen, H. Drury, S. Joshi, and M. Miller, "Functional and structural mapping of human cerebral cortex: Solutions are in the surfaces," 1998.

[96] L. Wang, B. N. Makouei, D. M. Barch, M. F. Beg, and M. Miller, "More Accurate Registration of Hippocampal Functional Data via Large-Deformation Differomorphic Maps," *Proceedings of the Human Brain Mapping*, 2006.

[97] W. Wells, P. Viola, H. Atsumi, S. Nakajima, and R. Kikinis, "Multi-modal volume registration by maximization of mutual information," *Medical Image Analysis*, vol. 1, no. 1, pp. 35–51, 1996.